

Thermal Effects of Thin Igneous Intrusions on  
Diagenetic Reactions in a Tertiary Basin of  
Southwestern Washington

U.S. GEOLOGICAL SURVEY BULLETIN 2085-C



**Cover.** Steeply dipping beds (fluvial channel deposits) of the Eocene Puget Group in the upper part of the Green River Gorge near Kanaskat, southeastern King County, Washington. Photograph by Samuel Y. Johnson, July 1992.

# Thermal Effects of Thin Igneous Intrusions on Diagenetic Reactions in a Tertiary Basin of Southwestern Washington

By Kenneth J. Esposito *and* Gene Whitney

EVOLUTION OF SEDIMENTARY BASINS—CENOZOIC SEDIMENTARY BASINS  
IN SOUTHWEST WASHINGTON AND NORTHWEST OREGON

Samuel Y. Johnson, Project Coordinator

---

U.S. GEOLOGICAL SURVEY BULLETIN 2085-C

*A multidisciplinary approach to research studies of sedimentary rocks and their constituents and the evolution of sedimentary basins, both ancient and modern*



UNITED STATES GOVERNMENT PRINTING OFFICE, WASHINGTON : 1995

**U.S. DEPARTMENT OF THE INTERIOR**

**BRUCE BABBITT, Secretary**

**U.S. GEOLOGICAL SURVEY**

**Gordon P. Eaton, Director**

For sale by U.S. Geological Survey, Information Services  
Box 25286, Federal Center  
Denver, CO 80225

Any use of trade, product, or firm names in this publication is for descriptive purposes only and does not imply endorsement by the U.S. Government

**Library of Congress Cataloging-in-Publication Data**

Esposito, Kenneth J.

Thermal effects of thin igneous intrusions on diagenetic reactions in a Tertiary basin of southwestern Washington/by Kenneth J. Esposito and Gene Whitney.

p. cm.—(Evolution of sedimentary basins—Cenozoic sedimentary basins in southwest Washington and northwest Oregon; C)

(U.S. Geological Survey bulletin; 2085)

Includes bibliographical references.

Supt. of Docs. no.: I 19.3:2085C

1. Intrusions (Geology)—Washington (State). 2. Diagenesis—Washington (State).  
3. Geology, Stratigraphic—Tertiary. 4. Geology—Washington (State). I. Whitney,  
Gene. II. Title. III. Series. IV. Series: U.S. Geological Survey bulletin; 2085.

QE75.B9 no. 2085-C

[QE611.5.U6]

557.3 s—dc20

[552'.5]

94-23449

CIP

# CONTENTS

Abstract.....	C1
Introduction .....	1
Tectonic History .....	2
Thermal History.....	2
Stratigraphy .....	2
Previous Work on the Illitization Reaction .....	4
Mineralogy of Illite-Smectite .....	5
Illitization in Contact Metamorphic Environments .....	5
Materials and Methods .....	7
Sample Acquisition and Preparation .....	7
Clay-Mineral Analysis.....	7
X-Ray Fluorescence Spectrometry.....	8
Scanning Electron Microscopy.....	8
Petrographic Thin-Section Examination .....	8
Vitrinite Reflectance.....	8
Results .....	8
Petrography of Igneous Rocks.....	8
Diagenesis of Sedimentary Rocks .....	9
Clay-Mineral Composition .....	9
Variation in Illite-Smectite Expandability.....	9
Variation in Other Clay Minerals .....	10
Variation in Vitrinite Reflectance.....	11
Heat-Flow Calculations .....	11
Discussion.....	22
Reaction Kinetics.....	22
Factors Affecting Illitization Reaction Rates .....	25
Calculations of the Extent of the Illitization Reaction .....	25
Conduction, Diffusion, and Advection Near Intrusions .....	29
Paragenesis of Other Minerals.....	29
Summary and Conclusions .....	34
References Cited.....	34
Appendix .....	37

## FIGURES

1. Map of western Washington showing coal rank of Eocene macerals and location of cores examined for study.....	C3
2. Chart showing simplified Tertiary stratigraphy in the Puget Lowland.....	4
3. Diagram showing sample locations and distribution of rock types in cores .....	6
4. X-ray diffraction pattern showing peak positions used for determining illite-smectite expandability .....	7
5. Diagram showing igneous rock identification in terms of total alkalis and silica for samples in study.....	10
6. Schematic sections of cores WC-83-5 and WC-83-6 showing position of igneous rocks.....	11
7. Diagram showing point-count data and percentage of illite in illite-smectite, core WC-83-6 .....	12
8. Graph showing expandability of illite-smectite, core WC-83-6 .....	20
9. Scanning electron micrograph showing typical morphology of illite-smectite.....	21
10. Graph showing expandability of illite-smectite, core WC-83-5 .....	21
11. Graph showing percentages of kaolinite and chlorite, core WC-83-6 .....	21

12.	Scanning electron micrograph of kaolinite .....	23
13.	Scanning electron micrograph showing chlorite replacing biotite .....	23
14-17.	Graphs showing calculated temperature at various times after emplacement:	
14.	Between intrusions 6 and 3 m thick .....	24
15.	Of intrusions in core WC-83-6 .....	24
16.	Of 26-m-thick intrusion in core WC-83-5 .....	24
17.	Of 61-m-thick intrusion in core WC-83-5 .....	24
18.	Graph showing calculated illitization reaction extent using only the heat provided by intrusions matching observed illitization near the intrusions or at the midpoint between the intrusions .....	27
19-30.	Graph showing comparison of calculated and observed percent illite in illite-smectite for core:	
19.	WC-83-6 using 900°C intrusions for calculations .....	27
20.	WC-83-6 using 1,000°C intrusions for calculations .....	27
21.	WC-83-6 using 1,100°C intrusions for calculations .....	28
22.	WC-83-6 using 1,200°C intrusions for calculations .....	28
23.	WC-83-5 using 26-m-thick, 900°C intrusion for calculations .....	30
24.	WC-83-5 using 26-m-thick, 1,000°C intrusion for calculations .....	30
25.	WC-83-5 using 26-m-thick, 1,100°C intrusion for calculations .....	31
26.	WC-83-5 using 26-m-thick, 1,200°C intrusion for calculations .....	31
27.	WC-83-5 using 61-m-thick, 900°C intrusion for calculations .....	32
28.	WC-83-5 using 61-m-thick, 1,000°C intrusion for calculations .....	32
29.	WC-83-5 using 61-m-thick, 1,100°C intrusion for calculations .....	33
30.	WC-83-5 using 61-m-thick, 1,200°C intrusion for calculations .....	33

## TABLES

1.	Lithological and clay mineralogical data and distance to adjacent igneous intrusions for samples from core WC-83-6 .....	C13
2.	Lithological and clay mineralogical data and distance from pluton for samples from core WC-83-5 .....	16
3.	Lithological and clay mineralogical data for samples from core WC-83-17 .....	18
4.	Mean vitrinite reflectance values for samples from cores WC-83-5, WC-83-6, and WC-83-17 .....	20
5.	Mathematical relationships for heat-flow calculations .....	20
6.	Values for variables used in heat-flow calculations .....	22
7.	Published kinetic values used in the Arrhenius equation for activation energy and pre-exponential function during illitization .....	26
8.	Kinetic values used for activation energy and pre-exponential function to calculate illitization .....	29

# Thermal Effects of Thin Igneous Intrusions on Diagenetic Reactions in a Tertiary Basin of Southwestern Washington

By Kenneth J. Esposito *and* Gene Whitney

## ABSTRACT

Tertiary sedimentary rocks in the Puget Lowland of southwestern Washington are intruded by thin igneous sills that increase in both thickness and frequency toward the Cascade Mountains. Shale, mudstone, and sandstone were sampled from three drill cores: the core nearest the Cascades contains four basaltic sills in a 244-m-thick (800 ft) section, the second contains a single basaltic sill in a 457-m-thick (1,500 ft) section, and the third contains no igneous sills. Detailed clay-mineral analyses were performed to assess the thermal influence of these igneous intrusions on illitization and other clay-mineral reactions in the sedimentary rocks.

The extent of illitization is a function of temperature, which depends on maximum burial depth and proximity to intruded sills. In the two cores that contain intrusions, temperatures resulting from burial to a depth of about 4 km and a geothermal gradient of 35°C/km have produced interstratified illite-smectite with about 60–70 percent illite layers. The abundance of illite in illite-smectite increases to about 75–95 percent immediately adjacent to sills. Furthermore, the extent of the reaction (or percentage of illite layers in illite-smectite) is proportional to the thickness of the sill. The third core, which is farthest from the Cascade Range, contains no sills and has never been deeply buried, and only highly smectitic illite-smectite is present.

Modeling of the illitization reaction using conductive heat-flow calculations and reaction kinetics confirms that the extent of the illitization reaction as a result of heating by the sills diminishes rapidly away from the sill contact. The intrusions affect the surrounding rocks to a distance roughly equivalent to the thickness of the sill.

## INTRODUCTION

Smectite converts to illite via mixed-layer illite-smectite in both natural and experimental systems under the influence of increased temperature, and the proportion of smectite layers decreases as the reaction progresses (Perry

and Hower, 1970; Eberl and Hower, 1976; Hower and others, 1976; Boles and Franks, 1979; Pytte, 1982; Inoue and Utada, 1983; Ramseyer and Boles, 1986; Buhmann, 1992; Inoue and others, 1992; Velde and Vasseur, 1992; Whitney, 1992). In natural systems, the heat that drives the smectite to illite reaction may come from burial, from circulating hydrothermal fluids, or from igneous bodies. For example, shale in sedimentary basins exhibits a systematic decrease in the percentage of smectite layers in the mixed-layer illite-smectite (illite-smectite) with increasing temperature during burial (see, for example, Perry and Hower, 1970; Hower and others, 1976; Boles and Franks, 1979; Velde and Vasseur, 1992). Similar clay-mineral reactions result from contact metamorphism, manifested as a decrease in the expandability of illite-smectite near igneous intrusions (Pytte, 1982; Buhmann, 1992). It has been suggested that the illitization reaction can be used as a low-temperature geothermometer (Hoffman and Hower, 1979; Pollastro, 1993).

We investigated the effects of heat from intrusive rocks on the illitization reaction by examining clay-mineral reactions in sedimentary rocks near intrusions in a Tertiary basin in southwestern Washington. Samples of intrusive and host sedimentary rocks were obtained from three drill cores in Lewis, Pierce, and King Counties, southwestern Washington, between the Cascade Range and the Puget Lowland. The intrusive rocks are hosted by the fluvial-deltaic Puget Group, which consists dominantly of sandstone and siltstone and includes several thin beds of carbonaceous shale and coal. Several intrusive sills provide the basis for determining the extent to which the thermal maturity (increasing percentage of illite in illite-smectite) of the clays is dependent on the intercalated intrusions. Mineralogical and chemical characterizations of the clay minerals were used to establish illite-smectite composition as a function of distance from the intrusions. Conductive heat-flow modeling of the intrusions provided a heating profile in the country rock that was then combined with published kinetic expressions for the illitization reaction to determine the extent to which observed thermal maturity patterns resulted from heating effects of the thin intrusions.

*Acknowledgments.*—This research was funded by the U.S. Geological Survey Evolution of Sedimentary Basins Program. We thank Weyerhaeuser Corporation, and particularly Peter Hales, for access to cores. Sam Johnson provided guidance in sampling and geologic background for the study. Vito Nuccio provided the vitrinite reflectance data. We thank Sam Johnson and Rich Pollastro for constructive reviews.

## TECTONIC HISTORY

The geology of western Oregon and Washington exhibits the complex structural, lithological, and sedimentological relationships characteristic of colliding plate boundaries. During the Paleocene, low-angle subduction of the Kula and Farallon oceanic plates under the westward-moving North American plate (Ewing, 1980) created the Challis volcanic arc system, which extended from Idaho to the Dakotas (Nilsen and McKee, 1979). The configuration of this subduction changed in the late Paleocene when basaltic rocks of the Crescent Formation and the Siletz River Volcanics were erupted as seamounts along the continental margin. The Crescent Formation and the Siletz River Volcanics form the basement of the Oregon and Washington Coast Range. Published models for the origins of these rocks suggest that (1) they formed in an intracontinental rift setting somewhat analogous to the volcanism in the Andaman Sea and the Gulf of California (Wells and others, 1984; Snively, 1988; Babcock and others, 1992) or (2) they formed on a spreading center between the Kula and Farallon plates and were subsequently accreted to the continental margin by plugging of a subduction zone that resulted in the initiation of a new subduction zone to the west (Wells and others, 1984; Duncan and Kulm, 1989). The intracontinental rift model predicts that the eastern boundary of the rift province is a dextral strike-slip fault, consistent with the observations of Johnson (1984, 1985) and Johnson and Yount (1992) concerning the structural and subsidence histories of sedimentary basins in western Washington.

Pre-Tertiary metasedimentary rocks form the basement of the Cascade block east of the Coast Range in southern Washington. The structural boundary between the Cascade and Coast Range provinces extends northward through the southeastern Puget Lowland. This boundary is covered by Oligocene and younger deposits but on the basis of geophysical data (gravity, magnetics, magnetotellurics) (S.Y. Johnson, oral commun., 1993) is inferred to be about 10–20 km (6.2–12.4 mi) west of the borehole sites examined in the study. Eocene sedimentary basins east of this boundary were characterized by rapid subsidence associated with transtension and sedimentary fill as thick as 6,000 m (20,000 ft) (Johnson, 1985; Johnson and Yount, 1992). The rocks of the Puget Group examined for this study make up a part of this thick sedimentary fill.

In the latest Eocene or early Oligocene, following a significant tectonic transition along the continental margin, the Cascade volcanic arc was initiated. Since that time, the Cascade foothills and Coast Range province have occupied part of the Cascade forearc basin. Since the Eocene, the region has also experienced significant heterogeneous (decreasing to the east) clockwise rotation (as much as 75°). Several causes of rotation have been suggested (Wells and Heller, 1988), including oblique subduction of the oceanic plates against North America, block rotations between parallel and subparallel transcurrent faults, and basin and range extension.

## THERMAL HISTORY

The thermal history of western Washington has been inferred primarily from the distribution of indicators of thermal maturity in the sedimentary rocks in the region. Mean vitrinite reflectance of coal macerals is one of the primary methods for estimating thermal maturity of sedimentary rocks that contain organic matter (Waples, 1985). Coals in the Puget Lowland of Washington are mostly lignite and subbituminous, but coal rank increases eastward toward the Cascades, where coals are low-volatile bituminous or anthracite (Walsh and Lingley, 1991) (fig. 1). Walsh and Lingley (1991) related the regional increase in coal rank toward the Cascades to the elevated heat flow associated with late Oligocene to middle Miocene intrusive activity in the Cascade arc. They suggested that this elevated heat flow affected coal rank for a distance of several kilometers. In addition to heating from burial and nearby intrusions, other areas in the Pacific Northwest also show local evidence for convective heating by hydrothermal fluids (Summer and Verosub, 1989). Unfortunately, coal beds are not distributed with sufficient regularity or frequency to map heat flow in any greater detail than at a regional scale.

## STRATIGRAPHY

Our research focused on the thermal effects of igneous intrusions on the sedimentary rocks of the Puget Group. Because of the complex geology, formation names change in different geographic areas, and a simplified stratigraphic section of local Tertiary formations is represented in figure 2.

The geology in the study area, was first described in detail by Fisher (1957, 1961). The sedimentary rocks in the area are lithologically similar to the Puget Group to the north in the Black Diamond area where isotopic and paleontologic dates and stratigraphic relationships indicate a middle to late Eocene age (Vine, 1962; Turner and others, 1983; Frizzell and others, 1984). The Puget Group consists of predominantly feldspathic sandstone and siltstone and lesser

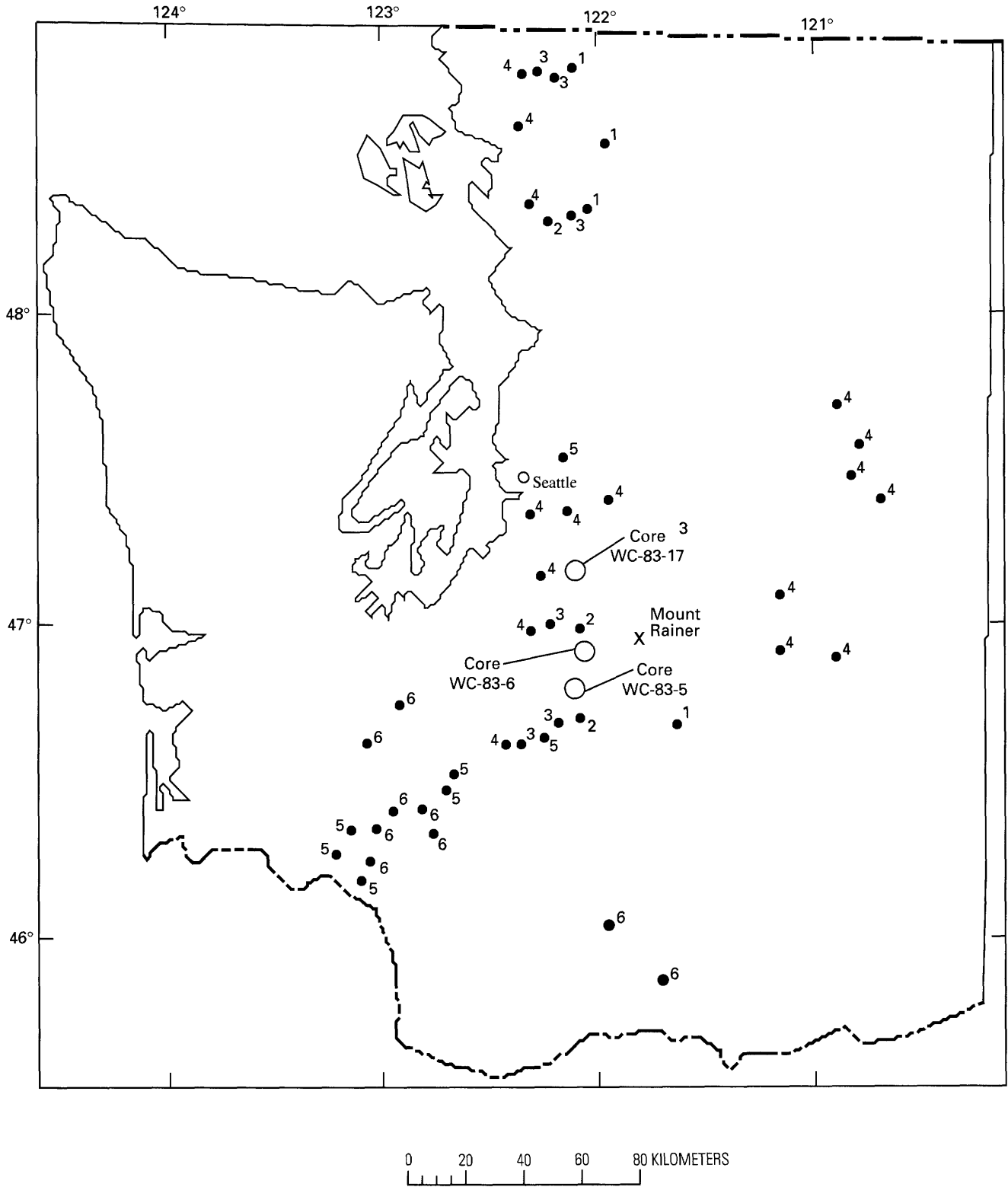


**Figure 1.** Map of western Washington showing coal rank of Eocene macerals and location of the three cores examined for this study. Core WC-83-17 is in King County, sec. 13, T. 22 N., R. 6 E.; core WC-83-6 is in Lewis County, SW $\frac{1}{4}$  sec. 29, T. 14 N., R. 5 E.; and core WC-83-5 is in Pierce County, sec. 28, T. 15 N., R. 6 E. Coal rank of Eocene macerals (solid circles; from Walsh and Phillips, 1983) is indicated by number: 1, anthracite; 2, low volatile bituminous; 3, medium volatile bituminous; 4, high volatile bituminous; 5, subbituminous; 6, lignite.

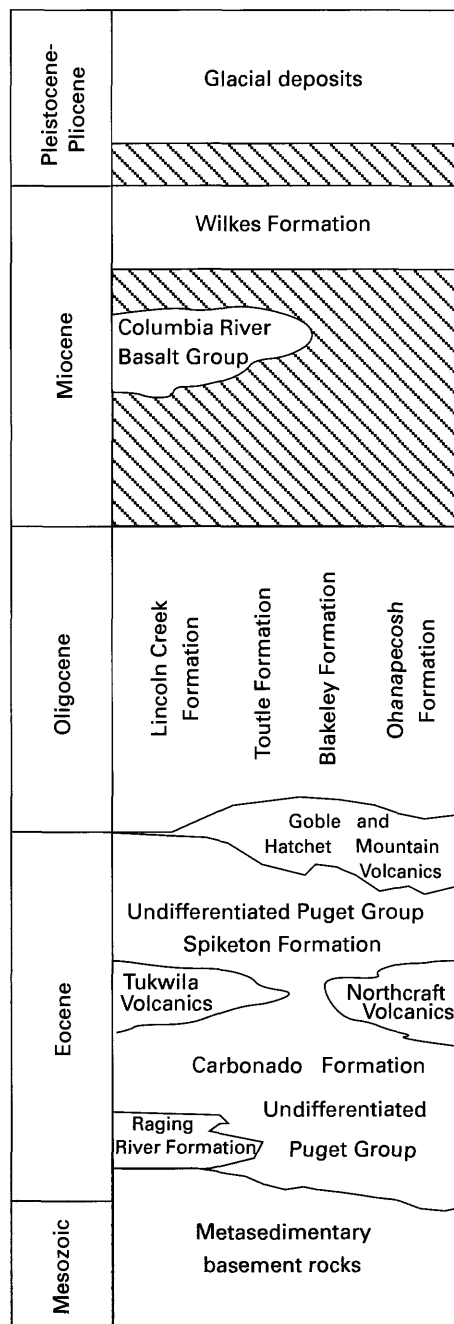


**Figure 2.** Simplified Tertiary stratigraphy in the Puget Lowland in the Seattle and Carbon River areas. Modified from Armentrout and others (1983).

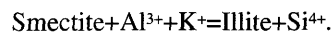
amounts of carbonaceous shale and coal. It was deposited in a variety of fluvial-deltaic environments including prodelta, delta front, interdistributary bay, swamp, fluvial distributary channel, natural levee, and braided stream (Buckovic, 1979; Evans, 1989). Igneous dikes, sills, and flows of varying compositions and thicknesses are present in the sedimentary

sequence (Fisher, 1961). The Puget Group includes several formations, including the Carbonado and Spiketon Formations (Armentrout and others, 1983). Rocks from the two southern cores of this study (fig. 1) are probably part of the Carbonado Formation, whereas the northern core contains undifferentiated upper Puget Group rocks correlative with the Spiketon and Skookumchuck Formations (S.Y. Johnson, oral commun., 1993).

## PREVIOUS WORK ON THE ILLITIZATION REACTION

The illitization reaction, in which smectite is converted to illite via an intermediate mixed-layer illite-smectite, has been observed and studied in burial diagenetic settings (Perry and Hower, 1970; Hower and others, 1976; Boles and Franks, 1979; Velde and Vasseur, 1992), in contact metamorphic environments (Pytte, 1982; Ramseyer and Boles, 1986; Buhmann, 1992), and during hydrothermal fluid migration (Inoue and Utada, 1983; Inoue and others, 1992). It has also been studied experimentally (Eberl and Hower, 1976; Whitney and Northrop, 1988; Huang, 1992; Whitney, 1992; Whitney and Velde, 1993) to provide a better understanding of the reaction mechanism and processes in natural systems.

The basic reaction of smectite to illite can be written:



The exact mechanism of the reaction from smectite to illite is poorly understood and has been the subject of considerable research. Several mechanisms have been proposed including a solid-state reaction (Hower and others, 1976), neoformation and crystal growth (Nadeau and others, 1985; Yau and others, 1987; Inoue and others, 1988; Eberl and others, 1990), interlayer dissolution (Altaner, 1989), and smectite cannibalization (Boles and Franks, 1979).

In the solid-state reaction model, phyllosilicate layers remain intact (do not completely dissolve) as ionic substitutions within the low-charge smectite layers produce high-charge illite layers (Weaver and Beck, 1971; Hower and others, 1976). The layer charge is built by ionic substitution of aluminum for silicon in the tetrahedral sheet and (or) magnesium for aluminum in the octahedral sheet. As the negative charge on the layers increases, electrical balance is maintained by the addition of interlayer potassium ions. When the layer charge increases to about 0.7 equivalents per  $\text{O}_{10}(\text{OH})_2$ , water is driven off and the interlayer potassium becomes fixed, transforming a smectite layer to an illite layer. In the solid-state model, ions are supplied by the dissolution of potassium feldspar or other accessory phases. This model has been suggested for the early formation of

disordered illite-smectite during illitization (Inoue and others, 1987; Whitney and Northrop, 1988).

Two models rely on the complete dissolution of smectite layers as illitization proceeds. The neoformation and crystal growth model proposes that decreased expandability of illite-smectite results from the dissolution of thin unstable smectite crystallites and the subsequent crystallization of thin illite crystallites, which themselves dissolve and grow into larger illite crystals. An increase in particle thickness (more 2:1 layers in each crystallite; Eberl and Srodon, 1988) and lateral dimensions (each 2:1 layer growing in the *a* and *b* crystallographic directions; Inoue and others, 1988) of illite-smectite suggests that illite recrystallization occurs by an Ostwald ripening process in which small illite particles dissolve and nourish the growth of larger illite particles. Nadeau and others (1984) showed that large illite-smectite particles grow larger at the expense of dissolving smaller particles. Similarly, the smectite cannibalization model proposes that dissolution of the smectite layers provides all of the aluminum needed for the reaction to proceed; no external source of aluminum is needed because aluminum is conserved (Boles and Franks, 1979; Pollastro, 1985).

In the interlayer dissolution model, parts of adjacent smectite 2:1 layers dissolve and recrystallize around the interlayer space as an illite layer, and the remaining parts of the smectite 2:1 layers are unaffected (Altaner, 1989; Altaner and Ylagan, 1993). Transmission electron microscopy (TEM) studies (Ahn and Peacor, 1986) suggest that illite-smectite can be thought of as a stack of high-charge (illite) and low-charge (smectite) interlayers such that an individual 2:1 layer can have a high-charge tetrahedral sheet on one side and a low-charge tetrahedral sheet on the other. This model, in essence, proposes the dissolution of the low-charge half of the 2:1 layer and reprecipitation of a high-charge tetrahedral sheet. Research by Drits (1987) demonstrates that the reaction of smectite to illite is accompanied by redistribution of octahedral cations, as well as by an increase in tetrahedral charge. Thus, if the interlayer dissolution model operates, the octahedral sheet must also be affected.

Although the reaction is written as if illite and smectite are in chemical equilibrium, the reaction is, for all practical purposes, irreversible. Because the reaction is believed to be controlled by reaction kinetics, both the maximum temperature and the duration of the heating event play crucial roles in extent of illitization (Ramseyer and Boles, 1986). Velde and Vasseur (1992) contended that the duration of heating is more important than maximum temperature in determining the reaction extent for burial lasting millions to tens of millions of years; however, for short time spans, the effects of maximum temperature on the illitization reaction is uncertain. Velde and Lanson (1993) believed that in the Salton Sea area temperature was the most important variable controlling

extent of illitization over time spans of  $10^4$ – $10^5$  years, although they concluded that in the Paris Basin short-lived heating due to an intrusion had little effect on the progress of the illitization reaction.

### MINERALOGY OF ILLITE-SMECTITE

Illite-smectite is composed of illite layers and smectite layers stacked together either randomly or regularly along the *c*-axis (Reynolds, 1980). As the illitization reaction proceeds, the expandability (percentage of smectite layers) in the illite-smectite decreases, and the arrangement of the layers exhibits increasing regularity in stacking order. In our study we used the Reichweite (or "reach back") terminology consistent with the method of expandability determinations (Srodon, 1980). During the early stages of illitization the few illite layers (I) formed are distributed randomly within a stack of the smectite layers (S). This disordered stacking is referred to as  $R=0$  and is seen in samples containing less than 60 percent illite layers. As illitization proceeds to about 60 percent illite layers, the random arrangement between the illite and smectite layers is lost, and each smectite layer is separated by one illite layer. The perfect alternation between illite layers and smectite layers (ISISIS) is expressed as  $R=1$  ordering. The mineral rectorite, in which each smectite layer is separated by an illite layer, is an example of  $R=1$  ordering.  $R=1$  ordering can persist through continued illitization until about 80–85 percent illite (15–20 percent expandable). As illitization continues beyond about 80 percent illite layers, each smectite layer is separated by three illite layers (ISIISI-IIISII), which is expressed as  $R=3$  ordering. In summary, as illitization proceeds the percentage of illite layers increases and ordering increases from random stacking ( $R=0$ ), to short-range ordered stacking ( $R=1$ ), to long-range ordered stacking ( $R=3$ ). In the present study, the term "percent illite" refers only to the percent illite in mixed-layer illite-smectite (100 percent–percent smectite), not to the percentage of discrete illite in the clay-size fraction, and the term "percent expandable" refers to the percentage of smectite layers in illite-smectite.

### ILLITIZATION IN CONTACT METAMORPHIC ENVIRONMENTS

The illitization reaction has been previously documented in contact metamorphic environments. Pytte (1982) detailed the smectite to illite reaction in contact-metamorphosed rocks of the Pierre Shale in south-central Colorado. A pattern of decreasing expandability with increasing temperature was observed in rocks that were heated to temperatures ranging from 70°C to 250°C for durations of approximately 10 years to 300 m.y.

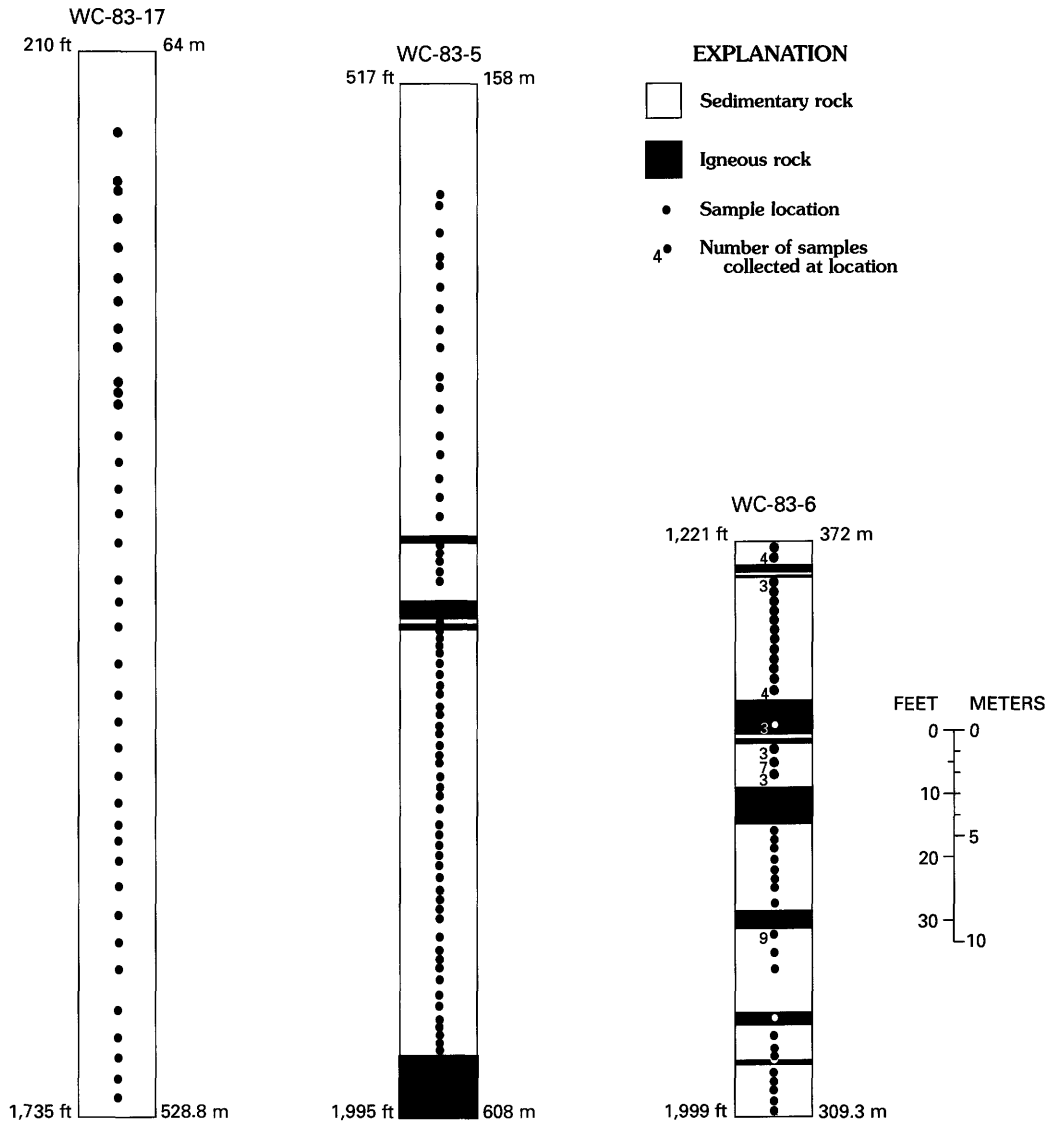
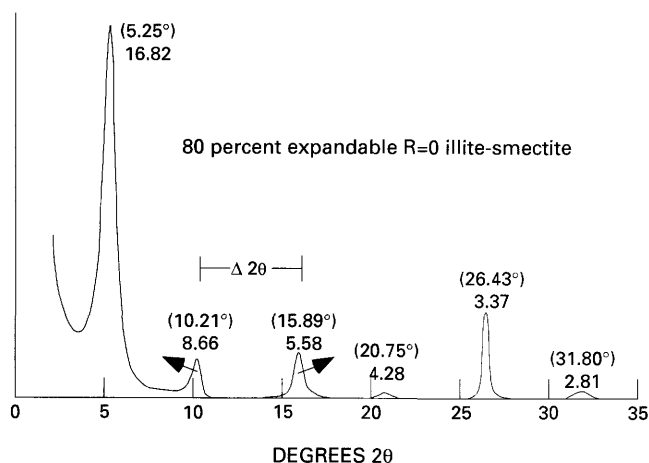


Figure 3. Sample locations and distribution of rock types in cores WC-83-5, WC-83-6, and WC-83-17.

Pytte suggested that the reaction is controlled by kinetic rather than equilibrium factors. He used measured expandabilities in lithologically homogenous sedimentary rocks to assign an activation energy to a sixth-order kinetic expression for the overall illitization reaction, first-order with respect to potassium availability and fifth-order with respect to starting smectite concentration. Pytte and Reynolds (1989) documented a zone of decreased expandability extending into the country rock a distance of approximately twice the intrusion thickness. They used the sixth-order model to explain the illitization process in the field and concluded that the correct kinetic rate law is probably a chain of low-order reactions, each having different kinetic constraints.

Buhmann (1992) identified obvious temperature-dependent trends in illite-smectite composition in the

vicinity of intrusive sills in the Karoo Basin in the Republic of South Africa. In contrast to the almost homogeneous Pierre Shale, Karoo Basin strata contain interbedded sandstone, siltstone, and carbonaceous mudstone. A systematic decrease in the expandability in illite-smectite from 70 to 5 percent was reported in the vicinity of the sills. Near the intrusion, where illitization proceeded to ordered phases ( $R=1$ ) of illite-smectite, correlation of illitization with vitrinite reflectance data was relatively good. Closer to the intrusion, higher ordering in illite-smectite ( $R>1$ ) corresponded to greater vitrinite reflectance values; however, farther from the intrusion, correlation of illitization with vitrinite reflectance values was poor because vitrinite reflectance values increased again, and highly expandable disordered illite-smectite ( $R=0$ ) predominated. Buhmann was unable to explain this discrepancy between vitrinite maturity



**Figure 4.** X-ray diffraction pattern of a mixed-layer illite-smectite containing 20 percent randomly interstratified illite layers. Peak positions are labeled by d-spacing and  $2\theta$  (in degrees) ( $\text{CuK}\alpha$  radiation). Arrows indicate direction of migration of peak positions as the percentage of illite layers increases. The difference between these two peaks ( $\Delta 2\theta$ ) is used for determining illite-smectite expandability.

and illite-smectite immaturity. In general, the effect of igneous intrusions on sedimentary rocks is primarily dependent on the proximity and thickness of the intrusion, although the distance over which changes can occur in illite-smectite composition may vary considerably with vitrinite reflectance values (Buhmann, 1992).

## MATERIALS AND METHODS

### SAMPLE ACQUISITION AND PREPARATION

This investigation was based on 117 sedimentary and 12 igneous rock samples collected from three cores, WC-83-5, WC-83-6, and WC-83-17 (fig. 1), which span 49 km (30 mi) of the Puget trough near the Cascade Range. They were collected at the Weyerhaeuser core storage facility in Dupont, Washington. Samples were taken at varying intervals from all three cores, with particular attention to the sandstone and shale adjacent to the intrusive rocks (fig. 3). The core closest to the Cascades, WC-83-6, contains eight igneous bodies (four intrusions and four flows) that have an average thickness of 4 m (13 ft) in 235 m (771 ft) of core. Core WC-83-6 was sampled between 372 and 609 m (1,221–1,999 ft) depth. The second core, WC-83-5, contains three flows, each about 3 m (10 ft) thick, and an igneous intrusion at least 26 m (85 ft) thick at the bottom of the core. This core was sampled between 158 and 608 m (517–1,995 ft) depth. In core WC-83-17, the farthest from the Cascades, there are no intrusions between the sampled depths of 64 and 529 m (210–1,735 ft.).

Whole-rock samples were ground in a corundum mortar and pestle to a size of 325 mesh and loaded into an

aluminum sample holder for randomly oriented powder X-ray diffraction (XRD) analysis (Moore and Reynolds, 1989). Separation of the  $<1\text{-}\mu\text{m}$  fraction was obtained by coarsely grinding samples in a jaw crusher (approximately 2-mm chips), followed by ultrasonic disaggregation and centrifugation. The  $<1\text{-}\mu\text{m}$  size fraction was separated at 1,000 rpm for 8.2 minutes (Jackson, 1969). Sodium hexametaphosphate (0.1 molal solution) was used to disperse flocculated samples. Oriented samples were prepared by Millipore filtration and transferred to glass slides (Polastro, 1982). The oriented clay samples were X-rayed both air-dried and ethylene glycol-saturated. Ethylene glycol solvation of the sample was achieved by exposure to ethylene glycol vapor for at least 8 hours at  $60^\circ\text{C}$ .

A total of 129 samples were analyzed for clay-mineral composition by XRD. Analyses were performed on an automated Siemens D500 diffractometer using  $\text{CuK}\alpha$  radiation at 30 milliamps and 40 kV. A curved graphite crystal monochromator was used on the diffracted side of the beam path. Routine scans were run from  $2^\circ$  to  $50^\circ$   $2\theta$ , at 2 seconds per step and 50 steps per degree. Selected samples were analyzed using much longer count times for detection and resolution of minor peaks.

### CLAY-MINERAL ANALYSIS

In an ethylene glycol-saturated, oriented sample, pure (100 percent expandable) smectite is identified by a basal (001) spacing of  $17\text{\AA}$  and a regular sequence of 00 $l$  reflections in the XRD pattern. Irregular basal 00 $l$  reflections are characteristic of interstratified clay minerals. Srodon (1980) developed XRD methods for precise identification of illite-smectite interstratification. We used the method of differential  $2\text{-}\theta$  ( $\Delta 2\theta$ ) to estimate expandability of the illite-smectite. In this method the precise measurement between the illite-smectite 001/002 peak (near  $9^\circ\text{--}10^\circ$   $2\theta$ ) and 002/003 peak (near  $17^\circ$   $2\theta$ ) is used to estimate the expandability of a given illite-smectite phase. (By convention the illite-smectite 001/002 peak refers to the mixed-layer composite peak; for example, the 002 reflection of smectite migrates toward the 001 peak of illite as illitization proceeds.) Figure 4 shows the peak positions and  $\Delta 2\theta$  measurements on an XRD pattern. Estimating the expandability using the  $\Delta 2\theta$  method has many advantages over single-peak position estimations. Because it is a differential measurement, it is relatively insensitive to goniometer alignment and sample placement problems (Moore and Reynolds, 1989). Expandability estimations are also enhanced because these two peaks shift in different directions as illite composition changes.

The measured expandability of illite-smectite includes analytical error from domain size effects (Srodon, 1980), generally on the order of 5 percent but sometimes as high as 30 percent, for the method used for this study. In addition to analytical error, precise determination of the peak

positions needed to measure expandability (with  $2\theta$  peaks near  $10^\circ$  and  $17^\circ$ ) is affected by large amounts of discrete illite with peaks at  $8.9^\circ$  and  $17.8^\circ$ . When a large amount of discrete illite is present, the illite-smectite peaks appear as shoulders on the larger illite peaks.

One-dimensional XRD patterns were calculated for several expandabilities as an independent verification of expandabilities estimated with the  $\Delta 2\theta$  method. Several calculated patterns were generated for specified expandabilities and then compared to actual data. All calculated XRD patterns were modeled using the commercially available program NEWMOD (Reynolds, 1985).

Relative abundances of kaolinite and chlorite as a function of depth were calculated as ratios from the intensity of their respective peaks. Percentages were calculated by dividing the intensity of the kaolinite or chlorite XRD peak against the combined intensity for both minerals. The 002 peak of kaolinite and the 004 peak of chlorite, both of which are near  $25^\circ 2\theta$ , were measured on oriented mounts. Although this provides only a gross semiquantitative measure of abundance, it does provide a means of detecting changes in relative abundance of the two minerals with depth. The rank of clay-mineral abundances given in tables 1, 2, and 3 was based on gross peak intensities in oriented mounts of the  $<1\text{-}\mu\text{m}$  size fraction.

### X-RAY FLUORESCENCE SPECTROMETRY

Major-element chemical analysis was performed on all igneous rocks for purposes of classification and on selected sedimentary rocks in an attempt to detect metasomatism. Chemical analyses were carried out on an ARL Model 8420+ wavelength-dispersive X-ray fluorescence spectrometer. Samples were prepared as fused glass beads, using a method modified from Tertian and Claisse (1982). Finely ground samples were mixed with lithium tetraborate in a flux to sample ratio of 10:1. The mixture was fused over a gas flame at  $1,200^\circ\text{C}$  for 30 minutes, then poured into a 50-mm mold and slowly cooled for several hours. Samples were analyzed for silicon, aluminum, phosphorus, potassium, calcium, magnesium, sodium, titanium, manganese, and iron (total iron as  $\text{Fe}_2\text{O}_3$ ) using conventional crystal and detector combinations. Each analysis consisted of averaging five repetitive counts of 10 seconds for each element. Loss on ignition was determined by heating samples to  $900^\circ\text{C}$  prior to glass bead preparation and measuring weight loss.

### SCANNING ELECTRON MICROSCOPY

Clay textures and the paragenetic relationships among the clay minerals were examined using a Cambridge Stereoscan electron microscope at 20 kV accelerating voltage, with a  $\text{LaB}_6$  crystal, operating at 3.1 nanoamps. Small chips (5–10 mm) were mounted on aluminum sam-

ple holders with epoxy and allowed to dry thoroughly. Samples were then sputter coated with gold for 2–4 minutes. Qualitative spot chemical analyses were obtained using a Tracor Northern 5500 energy-dispersive X-ray spectrometer.

### PETROGRAPHIC THIN-SECTION EXAMINATION

Conventional thin sections of the sedimentary rocks were prepared using blue-epoxy impregnation for porosity determination and potassium feldspar stain. Point-count analysis (350 points minimum) of sedimentary rocks was used to identify and quantify any postdepositional authigenic phase that replaced detrital grains or pore space. Thin sections from all of the igneous bodies (prepared without feldspar stain) were inspected to determine (1) if they are intrusive or extrusive and (2) a reasonable intrusion temperature. Due to the very fine grained nature of the groundmass (and extensive alteration), classification of igneous rocks based on mineral abundances in thin sections could not be determined. Classification was based on major-element chemical analysis as proposed by LeBas and others (1986) for volcanic rocks.

### VITRINITE REFLECTANCE

Vitrinite, a maceral derived from woody plant material, is common in coal and carbonaceous shale. Vitrinite reflectance is a measurement of the proportion of light reflected from a polished vitrinite grain. It is related to the degree of metamorphism of the vitrinite grain and can be directly converted to coal rank and petroleum generation.

One coal sample from core WC-83-6, three coal samples from core WC-83-17, and four coal samples from core WC-83-5 were prepared by crushing, mounting in epoxy on a microscope slide, planing off when hardened, and polishing. The mean vitrinite reflectance from randomly oriented indigenous vitrinite grains was determined using plane-polarized incident white light and a 546-nm monochromatic filter, in immersion oil, on a reflected light microscope with a nonrotating stage. Several measurements were made for each sample. The data were plotted on histograms for interpretation (but not included in this study).

## RESULTS

### PETROGRAPHY OF IGNEOUS ROCKS

The igneous rocks in the cores are composed predominantly of plagioclase feldspar that ranges in

composition from 45 to 65 percent anorthite (based on extinction angles and XRD). The larger phenocrysts of feldspar usually exhibit compositional zoning. Clinopyroxene and biotite are present in most samples in relatively low abundances.

Detailed mineralogical analysis of the igneous rocks in thin section was complicated by the presence of fine-grained matrix and abundant alteration. Two basic textures were used to separate rocks on the basis of intrusive or extrusive origin. Intrusive textures include fine- to medium-grained euhedral interlocking crystals. Extrusive textures include very few, fine-grained phenocrysts in a glassy devitrified matrix.

Alteration of the igneous rocks is pervasive in all but the largest intrusions. Carbonate and opaque oxide minerals replace phenocrysts and matrix. Chlorite replaces biotite in most samples, and chlorite replaces clinopyroxene in the most highly altered samples.

Precise petrographic identification of mineralogy was impossible because of the fine-grained nature of the intrusive rocks and the pervasive alteration. Classification, therefore, was based on chemical analyses (fig. 5). Although the pervasive alteration must have also had some effect on the chemical composition of these rocks (especially loss of the alkali metals), the chemical analyses provided a much more consistent classification than did petrographic identification. Based on total alkalis and silica content, a basaltic composition is indicated. Basaltic rocks can have intrusion temperatures as high as 1,200°C (Best, 1982). Figure 6 and appendix table 2 indicate that the igneous rocks are either intrusive (sills) or extrusive (flows).

## DIAGENESIS OF SEDIMENTARY ROCKS

Figure 7 shows the relationship between the percentages of replacement and authigenic minerals and proximity to the intrusive body for samples 60 through 65 from core WC-83-6. These samples were taken from a single continuous sandstone bed adjacent to an intrusion to minimize differences in facies, detrital mineralogy, porosity and fluid chemistry. Point-count analysis of thin sections was used to identify and quantify any postdepositional authigenic phase that replaced detrital grains or pore space. Carbonate replacement of framework grains and authigenic growth in pore spaces has occurred near the intrusion. Authigenic carbonate increases near the intrusion (fig. 7), and carbonate abundance decreases sharply in contact with the intrusion. XRD analysis failed to document this trend because of the small percentage of carbonate minerals in each sample; however, wherever carbonate was detected in the core by XRD, the

composition of the carbonate varied considerably and included calcite, dolomite, and siderite.

## CLAY-MINERAL COMPOSITION

Sample depths, hand-specimen descriptions, and mineral compositions of the <1- $\mu\text{m}$  size fraction are presented in tables 1, 2, and 3 for cores WC-83-6, -5, and -17, respectively. In the cores containing igneous intrusions, the <1- $\mu\text{m}$  fraction is dominated by illite-smectite that has variable expandability and ordering and also includes smaller amounts of kaolinite, chlorite, and mica. (In this study, any 10Å phase is called mica; muscovite, biotite, and sericite are present in most thin sections.) The core containing no intrusions (WC-83-17) contains similar clay-mineral assemblages, although the expandability of the illite-smectite is consistently high and in most samples pure smectite is present with no interstratified illite. Although all three cores contain a wide range of lithologies, there is no apparent correlation between relative clay-mineral abundance and lithological variables such as rock type or grain size.

## VARIATION IN ILLITE-SMECTITE EXPANDABILITY

Of primary importance in this study is the decrease in expandability of illite-smectite near intrusions. Figures 8 and 9 show illite-smectite expandability as a function of depth and proximity to intrusions. Near the midpoints between the intrusions in core WC-83-6 (fig. 8), the illite-smectite expandability levels out at a minimum of about 35 percent (65 percent illite in illite-smectite). Immediately adjacent to the intrusions, the percentage of illite in illite-smectite increases by at least 5 percent and in some samples by as much as 25 percent. The texture of the illite-smectite ranges from thin flakes to feathery blades, indicative of authigenic formation (fig. 9). The illite-smectite in core WC-83-5 is about 30 percent expandable (70 percent illite in illite-smectite) between the intrusions and exhibits a pronounced decrease in expandability near the large intrusion at the base of the sampled interval (fig. 10). Adjacent to the intrusion, only a few smectite layers remain (98 percent illite in illite-smectite).

In addition to increasing the percentage of illite in illite-smectite near the intrusions, ordering of the illite-smectite also increases in the vicinity of the intrusions. In the few instances where large intrusions (>8 m thick) are present, expandability is 10 percent or less, and ordering increases to  $R=3$ . Core WC-83-17, which contains no

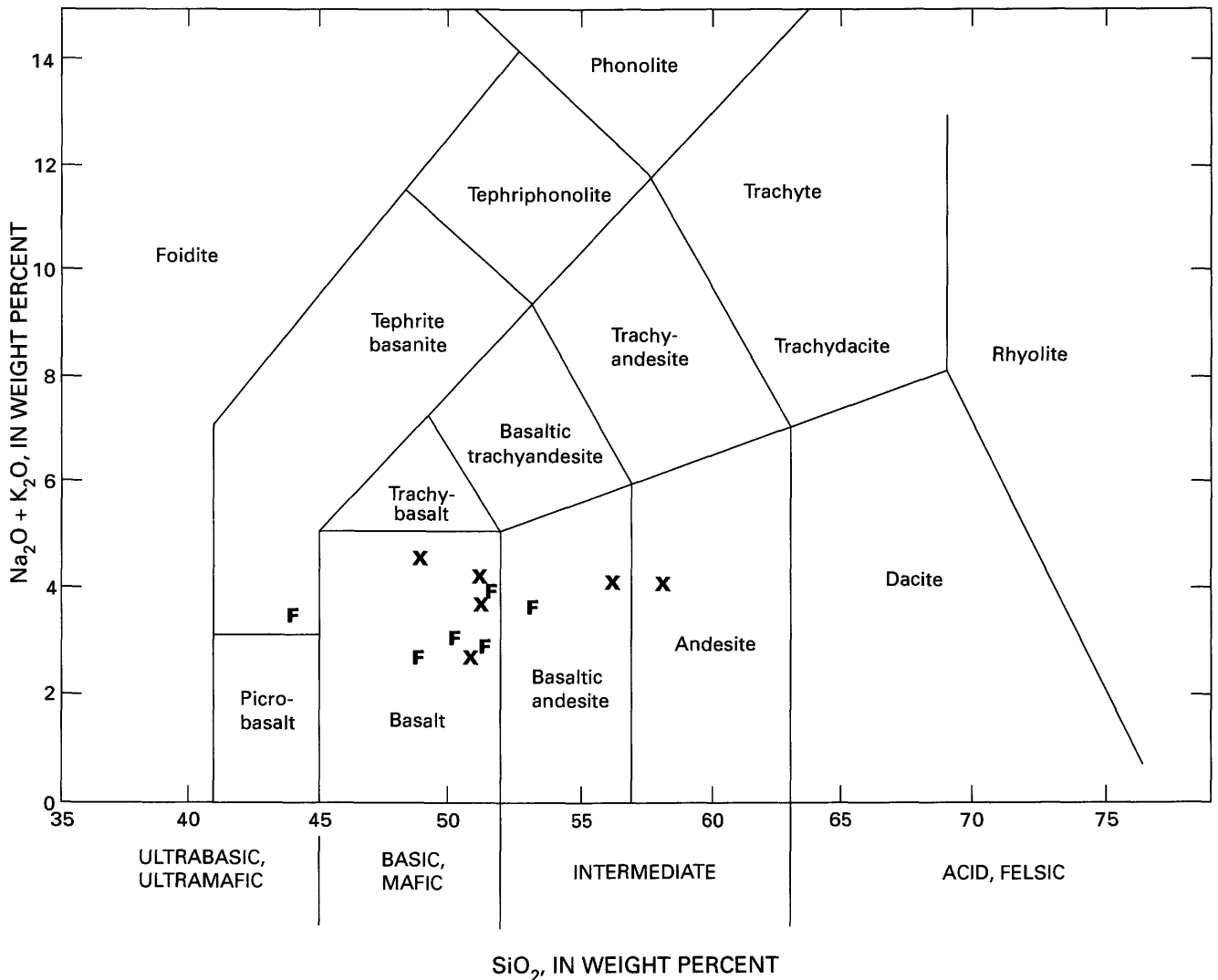


**Figure 5.** Igneous rock identification in terms of total alkalis and silica for samples in this study. Intrusive (x) and extrusive (F) determinations were made on the basis of petrographic observations. Sample information and analyses are given in appendix table 2. Classification modified from LeBas and others (1986).

intrusions, contains only very expandable illite-smectite: pure smectite is present throughout most of the core, although expandabilities decrease by 5–10 percent locally.

### VARIATION IN OTHER CLAY MINERALS

Although the clay mineralogy appears to be independent of lithology, the abundances of kaolinite and chlorite vary with vertical distance from intrusions within each core. Although there is a significant amount of scatter in the data, kaolinite decreases in abundance immediately near the intrusions (fig. 11), and chlorite increases in abundance. Kaolinite is present primarily as replacement of feldspar, and large authigenic kaolinite books were observed in thin section and using scanning electron microscope (fig. 12).

Based on texture and distribution, kaolinite probably is an alteration product that formed before the intrusive event. Emplacement of the intrusions may have led to dissolution of kaolinite near the intrusions.

In contrast to kaolinite, the proportion of chlorite shows an opposite trend: chlorite increases in the vicinity of the intrusions and decreases at increasing distances. Both in thin section and using scanning electron microscope, chlorite replaces mafic grains such as biotite. Scanning electron microscopy of the chlorite shows an authigenic texture that resembles delicate corn flakes when replacing a biotite grain (fig. 13). The relationship between the intrusions and chlorite and kaolinite content is not consistent throughout all cores, and the distribution of chlorite is not as well defined as that of kaolinite. Detrital mica (muscovite and biotite) probably has a distribution similar to that of kaolinite—most abundant away from the

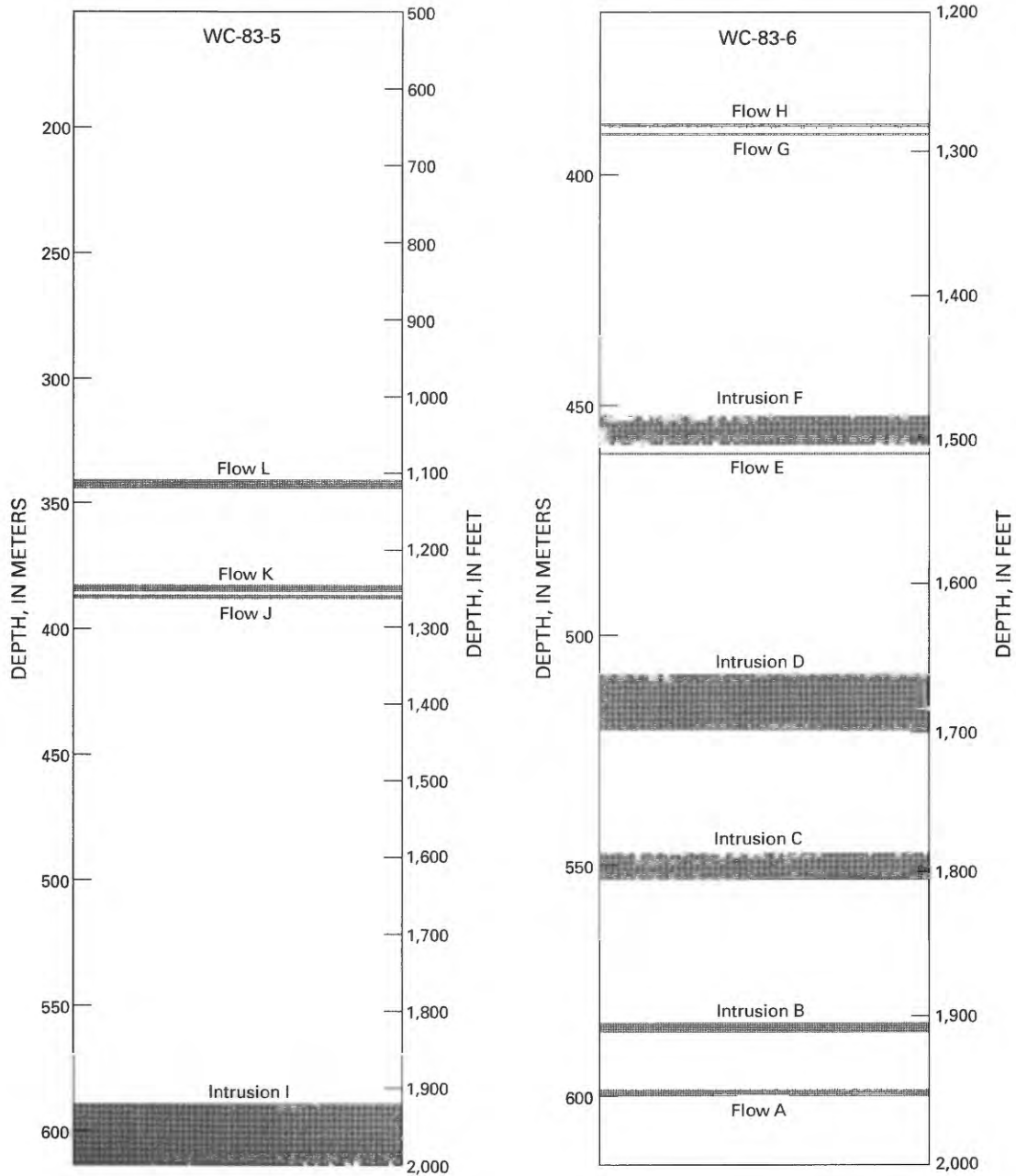


**Figure 6.** Position of igneous rocks in cores WC-83-5 and WC-83-6. Intrusive and extrusive determinations were made based on petrographic observations. Labels as to type correspond to those in tables 1 and 2 and appendix tables 1 and 2.

intrusions and least abundant near the intrusions. Based on dissolution features and the manner in which they are draped over other grains, the mica flakes probably are predominantly detrital.

**VARIATION IN VITRINITE REFLECTANCE**

Mean vitrinite reflectance values and observed illite-smectite expandability from cores WC-83-6 and WC-83-5 are shown in figures 8 and 10. Table 4 lists mean

vitrinite reflectance values (V. Nuccio, written commun., 1993) and core positions.

**HEAT-FLOW CALCULATIONS**

In order to evaluate whether the thin intrusions provide a reasonable heat source for the observed illitization, quantification of host-rock heating due to the intrusions is necessary. Modeling heat flow adjacent to a cooling

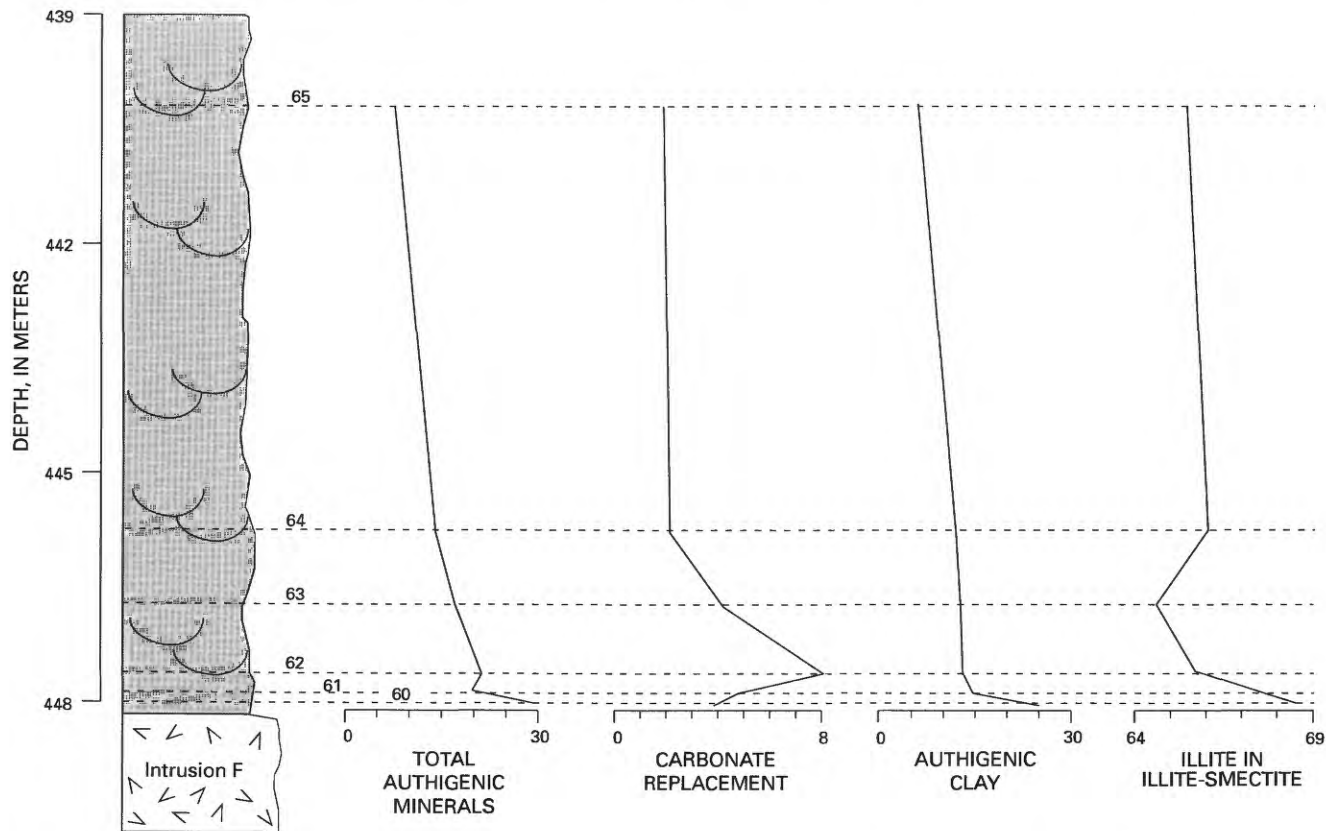


**Figure 7.** Point-count data (in percent) showing amounts of replacement and authigenic phases in rocks above a sill in core WC-83-6. Percentages of illite layers in illite-smectite are also shown. Numbers refer to sample numbers in table 1.

intrusion yields a time-temperature profile (Jaeger, 1964) that can be used to predict, if combined with an appropriate reaction rate expression, the extent of the illitization reaction as a function of distance from the intrusion. Heating was calculated for only those igneous bodies interpreted to be intrusions (fig. 6). The equations of Jaeger (1964, 1968) were used to calculate temperature profiles adjacent to igneous intrusions during the cooling process. The equations for the most common intrusive geometries are provided by Jaeger; thus, it is possible to calculate the temperature profile between two parallel sills (see also Furlong and others, 1991). These basic conductive heat-flow calculations provide a time-dependent temperature profile around the intrusions.

In order to manage the mathematics of heat-flow calculations, several simplifying assumptions were made. (1) The thermal conductivities and diffusivities of the country rock and the intrusion are approximately the same. (2) Intrusion is assumed to take place instantaneously, with no preheating of country rock. (3) The heat released by crystallization of the magma cannot be ignored, but it can be handled easily and accurately by increasing the initial temperature of the

magma (see following). (4) All thermal properties of both sedimentary and igneous rocks are assumed to be independent of temperature. This latter assumption may introduce the most error, but the effect of increasing temperature on the thermal diffusivity and conductivity of rocks is poorly understood. The importance of several complicating factors was assessed by Jaeger (1968), who concluded that errors associated with these assumptions have the greatest effect on the temperature profile inside the intrusion. Outside the intrusion, the general equations hold tolerably well. All dimensions (intrusion thickness, time after emplacement, and distance from contact) and thermal properties (thermal diffusivity and conductivity) are expressed in the two parameters  $\tau$  and  $\epsilon$  (Lovering, 1935). Table 5 summarizes Jaeger's (1964, 1968) mathematical relationships and defines the terms used in calculating the heating effect of intrusions. The temperature at any given point away from an intrusive sheet under deep cover can be expressed as a function of the parameters  $\epsilon, \tau$ . Because time, thermal diffusivity, and position relative to the intrusion are combined in this function, the approximate temperature at any point is the initial temperature multiplied by this function.

**Table 1.** Lithological and clay mineralogical data and distance to adjacent igneous intrusions for samples from core WC-83-6, sec. 28, T. 15 N., R. 6 E., Pierce County, Washington.

[Location of core hole shown in figure 1. Ordering of mixed-layer illite-smectite is given in Reichweite notation; parentheses denote trace amount of phase indicated. Mineralogy of <1- $\mu$ m fraction is given in order of abundance; illite-smectite is mixed-layer illite-smectite, chlorite-smectite is mixed-layer chlorite-smectite, and mica is muscovite or illite]

Sample number	Depth (feet)	Thickness of intrusion (feet)	Lithology	Percent illite in illite-smectite	Ordering	Mineralogy of <1- $\mu$ m fraction	Distance to closer intrusion (feet)	Distance to farther intrusion (feet)
85	1,263		Very fine grained sandstone and siltstone, ripple and horizontally laminated, bioturbated	26	R0	Illite-smectite, kaolinite, chlorite, mica, albite	11.0	
84	1,270.2		Carbonaceous mudstone	12	R0	Illite-smectite, kaolinite, chlorite	3.8	
83	1,271.6		Carbonaceous mudstone	45	R0	Illite-smectite, kaolinite, chlorite, mica, albite	2.4	
82	1,273.2		Carbonaceous mudstone	70	R1+(0)	Chlorite, illite-smectite, mica, albite	0.8	
81	1,273.8		Carbonaceous mudstone	67	R1	Illite-smectite, chlorite, mica, albite	0.2	
Flow H	1,276.5	8.4	Medium-grained light olive-gray, porphyritic					
80	1,282.5		Very fine grained sandstone and siltstone, ripple and horizontally laminated, bioturbated	70	R1	Illite-smectite, chlorite, mica, albite	0.1	188.0
79	1,283		Very fine grained sandstone and siltstone, ripple and horizontally laminated, bioturbated	20	R0	Illite-smectite, chlorite, mica	0.6	187.5
78	1,283.5		Very fine grained sandstone and siltstone, ripple and horizontally laminated, bioturbated	18	R0	Illite-smectite, kaolinite, chlorite, mica	1.1	187.0
77	1,305.2		Silty mudstone, olive-gray, massive	18	R0	Illite-smectite, kaolinite, chlorite, mica	22.8	165.3
76	1,313.6		Carbonaceous mudstone	21	R0	Illite-smectite, kaolinite, chlorite, jarosite	31.2	156.9
74	1,317.4		Silty mudstone, bioturbated	20	R0	Kaolinite, illite-smectite, chlorite, mica	35.1	153.1
73	1,318.8		Fine- to medium-grained sandstone, white, massive, bioturbated	60	R1+(0)	Kaolinite, illite-smectite, chlorite, mica	36.4	151.7
72	1,336		Very fine grained sandstone and siltstone, olive-gray, parallel-laminated, bioturbated	55	R1+0	Kaolinite, illite-smectite, chlorite, mica, albite	53.6	134.5
75	1,341		Fine-grained sandstone, olive-gray, ripple-laminated, bioturbated	40	R0	Kaolinite, illite-smectite, mica, chlorite, albite	58.6	129.5
71	1,353		Very fine grained sandstone and siltstone, olive-gray, ripple-laminated, bioturbated	50	R0+1	Kaolinite, illite-smectite, chlorite, mica, albite	70.6	117.5
70	1,353.5		Very fine grained sandstone and siltstone, olive-gray, ripple-laminated, bioturbated	60	R0+1	Illite-smectite, kaolinite, chlorite, mica, albite, calcite	71.1	117.0
69	1,362.5		Medium-grained sandstone, white, massive	65	R1	Kaolinite, illite-smectite, chlorite, mica, albite, calcite	80.1	108.0
68	1,378.5		Very fine grained sandstone and siltstone, ripple-laminated, dark-gray, bioturbated	59	R1+(0)	Illite-smectite, kaolinite, chlorite, mica, albite	92.0	96.1
67	1,400		Silty mudstone, olive-gray, massive	53	R0+(1)	Illite-smectite, kaolinite, mica, chlorite	70.5	117.6
66	1,402.8		Silty mudstone, olive-gray, massive	50	R0+1	Kaolinite, illite-smectite, mica, chlorite	67.7	120.4
65	1,446.8		Medium-grained sandstone, white, crossbedded	65	R1	Illite-smectite, chlorite, kaolinite, mica, albite	23.7	164.4
64	1,463.6		Medium-grained sandstone, white, crossbedded	65	R1	Illite-smectite, chlorite, mica, albite, calcite	6.9	181.2
63	1,466.5		Medium-grained sandstone, white, crossbedded	64	R1	Illite-smectite, chlorite, mica, albite	4.0	184.1
62	1,469.2		Medium-grained sandstone, white, crossbedded	64	R1	Illite-smectite, chlorite, mica, kaolinite, albite	1.3	186.8
61	1,470		Medium-grained sandstone, white, crossbedded	55	R1	Illite-smectite, chlorite	0.5	187.6

**Table 1.** Lithological and clay mineralogical data and distance to adjacent igneous intrusions for samples from core WC-83-6, sec. 28, T. 15 N., R. 6 E., Pierce County, Washington—Continued.

Sample number	Depth (feet)	Thickness of intrusion (feet)	Lithology	Percent illite in illite-smectite	Ordering	Mineralogy of <1- $\mu$ m fraction	Distance to closer intrusion (feet)	Distance to farther intrusion (feet)
60	1,470.4		Medium-grained sandstone, white, crossbedded	67	R1	Illite-smectite, chlorite, mica	0.1	188.1
Intrusion F	1,486.2	31.3	Fine grained, olive gray, porphyritic					
59	1,501.9		Medium-grained sandstone; spotted texture	69	R1	Illite-smectite, chlorite, mica, albite, calcite, cristobalite	0.1	163.6
58	1,503.3		Medium-grained sandstone; spotted texture	95	R3	Chlorite, illite-smectite, mica, kaolinite, albite, cristobalite, siderite, calcite	1.5	162.2
57	1,504.3		Medium-grained sandstone; spotted texture	10	R0	Chlorite, kaolinite, illite-smectite, mica, albite, cristobalite, calcite	2.5	161.2
56	1,506		Very fine grained to fine-grained sandstone and siltstone, massive, olive-gray	75	R1+0	Illite-smectite, chlorite, kaolinite, mica, albite	4.2	159.5
55	1,506.2		Very fine grained to fine-grained sandstone and siltstone, massive, olive-gray	65	R1	Illite-smectite, chlorite, mica, kaolinite, albite	4.4	159.3
54	1,507.2		Very fine grained to fine-grained sandstone and siltstone, massive, olive-gray	70	R1+(0)	Illite-smectite, chlorite, mica, kaolinite, albite	5.4	158.3
53	1,546.5		Clay-rich volcanic ash (?)	63	R0	Illite-smectite, chlorite, kaolinite, chlorite-smectite	44.7	119.0
52	1,554.8		Medium-grained sandstone, white; rare organic parallel-lamination	50	R0+(1)	Illite-smectite, chlorite, kaolinite, mica	53.0	110.7
51	1,558.5		Medium-grained sandstone, white; rare organic parallel-lamination	67	R1+(0)	Illite-smectite, kaolinite, chlorite, mica	56.7	107.0
50	1,578.7		Medium-grained sandstone, white; rare organic parallel-lamination	67	R1	Illite-smectite, chlorite, kaolinite, mica, albite	76.9	86.8
49	1,601		Medium-grained sandstone, white; rare organic parallel-lamination	67	R1+(0)	Illite-smectite, kaolinite, chlorite, mica, albite	64.5	99.2
48	1,611		Medium-grained sandstone, white; rare organic parallel-lamination	67	R1	Illite-smectite, kaolinite, chlorite, mica, albite, calcite, dolomite	54.5	109.2
47	1,613.3		Very fine grained sandstone and siltstone, parallel-laminated, bioturbated	60	R0 +1	Illite-smectite, kaolinite, chlorite, mica, albite	52.2	111.5
46	1,651		Fine-grained sandstone, ripple-laminated	67	R1	Illite-smectite, chlorite, kaolinite, mica, albite, dolomite	14.5	149.2
45	1,654.5		Very fine grained sandstone and siltstone, olive-gray, parallel-laminated, bioturbated	68	R1	Illite-smectite, chlorite, kaolinite, mica, albite	11.0	152.7
44	1,655.5		Very fine grained sandstone and siltstone, olive-gray, parallel-laminated, bioturbated	70	R1	Illite-smectite, mica, chlorite, kaolinite	10.0	153.7
Intrusion D	1,674.5	28	Medium-grained olive-gray					
43	1,700		Fine-grained sandstone, white, ripple-laminated	90	R3	Illite-smectite, mica, chlorite, albite	6.5	85.0
42	1,722.6		Fine-grained sandstone, white, ripple-laminated	65	R1+(0)	Illite-smectite, chlorite, kaolinite, mica, albite	29.1	62.4
41	1,743.5		Carbonaceous mudstone, bioturbated	64	R1	Illite-smectite, kaolinite, mica, chlorite, albite	41.5	50.0
40	1,760		Fine-grained sandstone, white, ripple-laminated	65	R1	Illite-smectite, chlorite, kaolinite, mica, albite	25.0	66.5

39	1,766	Fine-grained sandstone, white, ripple-laminated	70	R1+(0)	Illite-smectite, kaolinite, chlorite, mica, albite, calcite	19.0	72.5
38	1,768.8	Fine-grained sandstone, white, ripple-laminated	71	R1+(0)	Illite-smectite, chlorite, kaolinite, mica	16.2	75.3
37	1,769.8	Very fine grained to fine-grained sandstone and siltstone, finely laminated, bioturbated	68	R1+(0)	Illite-smectite, chlorite, mica	15.2	76.3
36	1,778	Carbonaceous mudstone	73	R1+0	Illite-smectite, chlorite, kaolinite, mica	7.0	84.5
Intrusion C	1,794.8	Medium-grained, greenish-gray	19.5				
35	1,804.5	Fine-grained siltstone and mudstone, olive-gray, bioturbated	65	R1	Illite-smectite, chlorite, mica, kaolinite, albite	0.0	91.5
34	1,805.3	Fine-grained siltstone and mudstone, olive-gray, bioturbated	67	R1	Illite-smectite, chlorite, kaolinite, mica	0.8	90.7
33	1,806	Fine-grained siltstone and mudstone, olive-gray, bioturbated	71	R1	Illite-smectite, chlorite, mica	1.5	90.0
32	1,807.3	Fine-grained siltstone and mudstone, olive-gray, bioturbated	73	R1+(0)	Illite-smectite, chlorite, kaolinite, mica	2.8	88.7
31	1,808.8	Fine-grained siltstone and mudstone, olive-gray, bioturbated	76	R1+(0)	Illite-smectite, chlorite, mica, kaolinite	4.3	87.2
30	1,810.8	Fine-grained siltstone and mudstone, olive-gray, bioturbated	70	R1+0	Illite-smectite, chlorite, kaolinite, mica	6.3	85.2
29	1,812.4	Fine-grained siltstone and mudstone, olive-gray, bioturbated	67	R1+0	Illite-smectite, kaolinite, chlorite, mica	7.9	83.6
28	1,814.7	Fine-grained siltstone and mudstone, olive-gray, bioturbated	68	R1+(0)	Illite-smectite, chlorite, kaolinite, mica	10.2	81.3
27	1,816.7	Fine-grained siltstone and mudstone, olive-gray, bioturbated	69	R1	Illite-smectite, kaolinite, chlorite, mica	12.2	79.3
26	1,828.4	Fine-grained siltstone and mudstone, olive-gray, bioturbated	65	R1+(0)	Kaolinite, illite-smectite, chlorite, mica, calcite, dolomite	23.9	67.6
25	1,854.8	Fine-grained siltstone and mudstone, olive-gray, bioturbated	70	R1+(0)	Kaolinite, illite-smectite, chlorite, mica, albite	41.2	50.3
Intrusion B	1,892	Medium grained, greenish gray	5	R0			
23	1,928.5	Fine-grained sandstone, greenish-gray, ripple-laminated	72	R1+(0)	Illite-smectite, kaolinite, chlorite, mica, albite	22.5	
22	1,940.7	Fine-grained sandstone, greenish-gray, ripple-laminated	67	R1+0	Illite-smectite, kaolinite, chlorite, mica	34.7	
21	1,943.7	Fine-grained sandstone, greenish-gray, ripple-laminated	60	R0	Illite-smectite, kaolinite, mica, chlorite	37.7	
19	1,953	Medium-grained sandstone, pale-orange, massive	69	R1+0	Illite-smectite, kaolinite, mica, chlorite	47.0	
18	1,962.8	Fine-grained sandstone, massive, bioturbated; roots	69	R1+(0)	Illite-smectite, kaolinite, chlorite, mica	56.8	
17	1,965.4	Fine-grained sandstone, pale-orange, ripple-laminated	69	R1	Illite-smectite, kaolinite, mica, chlorite	59.4	
16	1,991	Fine-grained sandstone, gray, ripple-laminated	72	R1	Illite-smectite, kaolinite, mica, chlorite	85.0	
15	1,999	Fine-grained sandstone, pale-orange, ripple-laminated	65	R1+(0)	Illite-smectite, kaolinite, mica, chlorite	93.0	

**Table 2.** Lithological and clay mineralogical data and distance from pluton for samples from core WC-83-5, SW¼ sec. 29, T. 14 N., R. 5 E., Lewis County, Washington. [Location of core hole shown in figure 1. Ordering of mixed-layer illite-smectite is given in Reichweite notation; parentheses denote trace amount of phase indicated. Mineralogy of <1-µm fraction is given in order of abundance; illite-smectite is mixed-layer illite-smectite, chlorite-smectite is mixed-layer chlorite-smectite, and mica is muscovite or illite]

Sample number	Depth (feet)	Thickness of intrusion (feet)	Lithology	Percent illite in illite-smectite	Ordering	Mineralogy of <1-µm fraction	Distance from pluton (feet)
224	513.4		Fine-grained sandstone, white, ripple-laminated	62	R1	Illite-smectite, kaolinite, mica, chlorite, albite, siderite, calcite	1,400.5
223	518.9		Bentonitic ash, white, massive	73	R1	Illite-smectite	1,395
222	538.4		Very fine grained to fine-grained sandstone, brownish-gray, bioturbated	71	R1	Illite-smectite, kaolinite, mica, chlorite, quartz	1,375.5
221	559		Siltstone and mudstone, brownish-gray, horizontally laminated	75	R1	Kaolinite, illite-smectite, mica	1,354.9
220	560		Siltstone and mudstone, brownish-gray, horizontally laminated	78	R1	Kaolinite, illite-smectite, mica, chlorite	1,353.9
219	590		Medium-grained sandstone, clean-white, laminated	78	R1	Illite-smectite, kaolinite, mica, chlorite	1,323.9
218	638.2		Sandstone and siltstone, dark-gray, parallel-laminated	73	R1	Illite-smectite, kaolinite, mica, chlorite, quartz	1,275.7
217	690		Siltstone and mudstone, brownish-gray, bioturbated; relict lamination	73	R1	Illite-smectite, kaolinite, mica, chlorite, quartz, albite	1,223.9
216	778.5		Fine-grained sandstone, white, ripple-laminated	72	R1	Illite-smectite, kaolinite, mica, chlorite, albite	1,135.4
215	824		Medium-grained volcanic ash, greenish-gray	68	R1	Illite-smectite, kaolinite, chlorite, mica, albite	1,089.9
214	828		Siltstone and mudstone, brownish-gray to black, laminated	73	R1	Kaolinite, illite-smectite, mica, chlorite, calcite, siderite	1,085.9
213	843		Very fine grained to fine-grained sandstone, brownish-gray, bioturbated	73	R1	Illite-smectite, kaolinite, mica, chlorite, albite, quartz	1,070.9
212	886.8		Medium-grained sandstone, white, laminated	71	R1	Chlorite, illite-smectite, mica, albite	1,027.1
211	914.3		Carbonaceous shale, coal	74	R1+(0)	Illite-smectite, chlorite, kaolinite, albite, mica, quartz	999.6
210	1,012.5		Medium-grained sandstone, greenish-gray	0		Smectite, calcite-siderite, chlorite, albite	901.4
209	1,059.7		Fine- to medium-grained sandstone, white, massive	74	R1	Illite-smectite, chlorite, mica, albite, kaolinite	854.2
207	1,097		Fine- to medium-grained sandstone, white, massive	76	R1+(0)	Illite-smectite, chlorite, mica, kaolinite	816.9
Flow L	1,120.5	10	Fine- to medium-grained intrusive rock, olive-gray	90	R3+(0)	Illite-smectite, chlorite, kaolinite	791.9
204	1,122		Very fine grained sandstone, olive-gray, massive	74	R1	Illite-smectite, chlorite, kaolinite, mica, albite, quartz	791.4
205	1,122.5		Very fine grained sandstone, olive-gray, massive	71	R1	Illite-smectite, chlorite, mica, kaolinite	790.9
206	1,123		Very fine grained sandstone, olive-gray, massive	73	R1	Illite-smectite, chlorite, mica, kaolinite	778.9
203	1,135		Fine-grained sandstone, gray, ripple lammed, bioturbated	75	R1+(3)	Chlorite, illite-smectite, mica, kaolinite	756.4
202	1,157.5		Medium-grained sandstone, white, massive; some rip-ups	80	R1+(3)	Illite-smectite, chlorite, kaolinite	642.7
Flow K	1,264.5	10.8	Fine- to medium-grained igneous rock, olive-black	90	R3	Illite-smectite, chlorite, kaolinite	636.4
201	1,271.2		Siltstone and mudstone, dark-gray, massive	78	R1	Illite-smectite, chlorite, mica, kaolinite, albite, quartz	632.4
Flow J	1,274.9	5.2	Fine- to medium-grained igneous rock, olive-black	90	R3	Illite-smectite, chlorite, kaolinite	
200	1,277.5		Siltstone and mudstone, olive-black, massive	78	R1	Illite-smectite, chlorite, mica, kaolinite, albite, quartz	
199	1,281.5		Very fine grained to fine-grained sandstone, olive-gray, massive	76	R1	Illite-smectite, chlorite, mica, albite, kaolinite	629.1
198	1,284.8		Very fine grained to fine-grained sandstone, olive-gray, massive	79	R1	Illite-smectite, chlorite, mica, albite, kaolinite	621.7
197	1,292.2		Very fine grained to fine-grained sandstone, olive-gray, laminated, bioturbated				

196	1,324	Fine-grained sandstone, white; organic lamination, some rip-ups	77	R3	Chlorite, illite-smectite, mica, kaolinite	589.9
195	1,374.5	Medium-grained sandstone, white; organic lamination, some rip-ups	90	R3	Illite-smectite, chlorite, mica, albite, kaolinite	539.4
194	1,443	Medium-grained sandstone, white; organic lamination, some rip-ups	83	R1+2(?)	Illite-smectite, chlorite, mica, albite	470.9
192	1,473.7	Sandstone and siltstone, dark-gray, laminated, some organics	70	R1	Illite-smectite, chlorite, kaolinite, mica, albite, quartz	440.2
190	1,571.5	Very fine grained sandstone, medium-gray, ripple-laminated, bioturbated	74	R1	Illite-smectite, kaolinite, mica, chlorite, albite, siderite	342.4
189	1,600.5	Fine-grained sandstone, white; some organic lamination	77	R1	Illite-smectite, kaolinite, mica, chlorite, albite, dolomite, siderite	313.4
188	1,634.3	Fine- to medium-grained sandstone; white; organic lamination	80	R1	Chlorite, illite-smectite, mica, albite	279.6
187	1,697.4	Fine- to medium-grained sandstone, white, massive	67	R1	Illite-smectite, chlorite, mica, kaolinite, albite, calcite	216.5
183	1,752	Fine-grained sandstone, white; some black organic lamination	74	R1	Illite-smectite, chlorite, kaolinite, mica, albite	161.9
182	1,766.5	Carbonaceous shale, coal	68	R1	Illite-smectite, mica, kaolinite, chlorite	147.4
181	1,821	Fine- to medium-grained sandstone, white-gray, flatbedded; organic lamination	78	R1	Illite-smectite, kaolinite, mica, chlorite	92.9
180	1,825.5	Siltstone and mudstone, gray, bioturbated	73	R1	Illite-smectite, kaolinite, mica	88.4
179	1,831.5	Siltstone and mudstone, gray, bioturbated	70	R1	Illite-smectite, kaolinite, mica, chlorite, siderite, quartz	82.4
178	1,835.5	Siltstone and mudstone, gray, bioturbated	69	R1	Illite-smectite, kaolinite, mica, chlorite, siderite, quartz	78.4
177	1,838	Siltstone and mudstone, gray, bioturbated	71	R1	Illite-smectite, kaolinite, mica, chlorite, siderite, quartz	75.9
176	1,842.2	Siltstone and mudstone, gray, bioturbated	72	R1	Illite-smectite, kaolinite, mica, chlorite, siderite, quartz	71.7
175	1,846.5	Siltstone and mudstone, gray, bioturbated	72	R1	Illite-smectite, kaolinite, mica, chlorite, quartz, siderite	67.4
174	1,849.2	Siltstone and mudstone, gray-black, parallel-laminated	73	R1	Illite-smectite, kaolinite, mica, chlorite, quartz, siderite	64.7
173	1,854.2	Siltstone and mudstone, gray-black, parallel-laminated	63	R1	Illite-smectite, kaolinite, mica, chlorite, quartz, siderite	59.7
172	1,857.2	Siltstone and mudstones, gray-black, parallel-laminated	63	R1	Illite-smectite, kaolinite, mica, chlorite, quartz	56.7
171	1,862.7	Siltstone and mudstone, gray-black, parallel-laminated	56	R1	Illite-smectite, kaolinite, mica, chlorite, quartz, siderite, pyrite	51.2
170	1,865.5	Siltstone and mudstone, gray-black, parallel-laminated	61	R1	Illite-smectite, kaolinite, mica, chlorite, quartz, siderite	48.4
169	1,870.5	Siltstone and mudstone, gray-black, parallel-laminated	59	R1	Illite-smectite, kaolinite, mica, chlorite, quartz, siderite	43.4
168	1,873.2	Siltstone and mudstone, gray-black, parallel-laminated	55	R1	Kaolinite, illite-smectite, mica, chlorite, siderite, pyrite, quartz	40.7
166	1,881.6	Siltstone and mudstone, gray-black, parallel-laminated	80	R1	kaolinite, illite-smectite, chlorite, siderite	32.3
165	1,885.6	Siltstone and mudstone, gray-black, parallel-laminated	95	R3	Illite-smectite, kaolinite, calcite-siderite, chlorite, quartz	28.3
167	1,887.3	Siltstone and mudstone, gray-black, parallel-laminated	64	R1	Kaolinite, illite-smectite, mica, chlorite, siderite, pyrite	26.6
164	1,889.6	Siltstone and mudstone, gray-black, parallel-laminated	95	R3	Kaolinite, illite-smectite, chlorite, chlorite-smectite, siderite, pyrite	24.3
163	1,893.5	Siltstone and mudstone, gray-black, parallel-laminated	61	R1	Illite-smectite, kaolinite, mica, chlorite, quartz, siderite	20.4
162	1,899.6	Siltstone and mudstone, gray-black, parallel-laminated	90	R3+(1)	Illite-smectite, kaolinite, chlorite-smectite, quartz, siderite, pyrite	14.3

**Table 2.** Lithological and clay mineralogical data and distance from pluton for samples from core WC-83-5, SW $\frac{1}{4}$  sec. 29, T. 14 N., R. 5 E., Lewis County, Washington—Continued.

Sample number	Depth (feet)	Thickness of intrusion (feet)	Lithology	Percent illite in illite-smectite	Ordering	Mineralogy of <1- $\mu$ m fraction	Distance from pluton (feet)
161	1,903.5		Siltstone and mudstone, gray-black, parallel-laminated	90	R3	Illite-smectite, kaolinite, calcite-siderite, quartz, siderite	10.4
160	1,906.5		Siltstone and mudstone, gray-black, parallel-laminated	95	R3+(1)	Illite-smectite, kaolinite, chlorite, quartz, siderite, pyrite	7.4
159	1,910		Mudstone, dark-gray	95	R3	Kaolinite, illite-smectite, chlorite, quartz, siderite	3.9
158	1,910.7		Mudstone, dark-gray			Kaolinite, siderite, quartz, chlorite, pyrite	3.2
157	1,912.2		Mudstone, dark-gray	98	R3	Illite-smectite, kaolinite, chlorite, quartz, siderite	1.7
156	1,913.8		Mudstone, dark-gray	98	R3	Illite-smectite, kaolinite, chlorite, quartz, siderite	0.1
Intrusion I	1,955.2	>84	Medium- to coarse-grained igneous rock, olive-black				

**Table 3.** Lithological and clay mineralogical data for samples from core WC-83-17, sec. 13, T. 22 N., R. 6 E., King County, Washington.

[Location of core hole shown in figure 1. Ordering of mixed-layer illite-smectite is given in Reichweite notation; parentheses denote trace amount of phase indicated. Mineralogy of <1- $\mu$ m fraction is given in order of abundance; illite-smectite is mixed-layer illite-smectite and mica is muscovite or illite]

Sample number	Depth (feet)	Lithology	Percent illite in illite-smectite	Ordering	Mineralogy of <1- $\mu$ m fraction
123	597.8	Very fine grained to fine-grained sandstone and siltstone, gray, parallel-laminated	<5	R0	Illite-smectite, kaolinite, chlorite, mica, quartz
122	635.5	Fine- to medium-grained sandstone, gray-white; some organic lamination	0		Smectite, kaolinite, chlorite, mica
121	637	Fine- to medium-grained sandstone, gray-white; some organic lamination	0		Smectite, chlorite, kaolinite, mica
120	730.7	Fine-grained sandstone and siltstone, parallel-laminated	7	R0	Illite-smectite, kaolinite, chlorite, mica, quartz
119	807	Very fine grained to fine-grained sandstone and siltstone, gray-white, massive	6	R0	Illite-smectite, kaolinite, chlorite, mica, quartz
118	840.4	Fine-grained sandstone and siltstone, parallel-laminated	0		Smectite, kaolinite, chlorite, mica
117	879.6	Very fine grained to fine-grained sandstone and siltstone, brown, parallel-laminated, bioturbated	0		Smectite, kaolinite, chlorite, mica
116	900.5	Carbonaceous mudstone	0		Smectite, kaolinite, chlorite, mica
115	902	Medium-grained sandstone, gray-white, massive	0		Smectite, kaolinite, chlorite, mica
114	905	Medium-grained sandstone, gray-white, massive	0		Smectite, kaolinite, chlorite, mica
113	934.7	Fine-grained sandstone and siltstone, gray, parallel-laminated, bioturbated	0		Smectite, kaolinite, chlorite, mica
112	998.2	Very fine grained to fine-grained sandstone and siltstone, gray, parallel-laminated	<5	R0	Illite-smectite, kaolinite, mica, chlorite
111	1,033.7	Mudstone (ash?)	0		Smectite, kaolinite, jarosite
110	1,053.8	Mudstone (ash?)	0		Smectite, kaolinite
109	1,092.6	Very fine grained to fine-grained sandstone and siltstone, gray, parallel-laminated, bioturbated	18	R0	Illite-smectite, kaolinite, chlorite, mica, jarosite, albite
108	1,112.4	Fine-grained sandstone and siltstone, gray-brown, massive, bioturbated	0		Smectite, kaolinite, chlorite, mica
107	1,136.2	Fine-grained sandstone, gray, massive; organic fragments	0		Smectite, mica, chlorite, kaolinite
106	1,146	Medium- to fine-grained sandstone, white, massive; near coal	0		Smectite, chlorite, kaolinite, mica
105	1,205.8	Medium-grained sandstone and siltstone, white; organic lamination	0		Smectite, kaolinite, mica
104	1,234.2	Medium-grained sandstone and siltstone, white; organic lamination	0		Smectite, kaolinite, mica

103	1,263.4	Fine-grained sandstone, gray, massive, bioturbated	5	R0	Illite-smectite, kaolinite, chlorite, mica, quartz
102	1,273.6	Fine-grained sandstone and siltstone, parallel-laminated, bioturbated	0		Smectite, kaolinite, chlorite, mica
101	1,292	Medium-grained sandstone, white, massive, mud rip-ups	0		Smectite, kaolinite, mica
100	1,307.5	Very fine grained to fine-grained sandstone and siltstone, gray, bioturbated; organic lamination	0		Smectite, kaolinite, chlorite, mica
99	1,328.3	Medium-grained sandstone, white, crossbedded; mud rip-ups	0		Smectite, kaolinite, mica
98	1,348.8	Carbonaceous mudstone	14	R0	Illite-smectite, kaolinite, mica, chlorite, jarosite, albite
97	1,406.3	Fine-grained sandstone, bioturbated; organic lamination	0		Smectite, kaolinite, mica
96	1,431	Carbonaceous mudstone	<5	R0	Illite-smectite, kaolinite, chlorite, mica
95	1,454	Very fine grained to fine-grained sandstone and siltstone, gray, massive, bioturbated	5	R0	Illite-smectite, kaolinite, chlorite, mica
94	1,467.8	Very fine grained to fine-grained sandstone and siltstone, gray, horizontally laminated, bioturbated	0		Smectite, kaolinite, chlorite, mica
93	1,508.3	Medium-grained sandstone, white, massive; mud rip-ups	0		Smectite, kaolinite, chlorite, mica
92	1,556.2	Medium-grained sandstone, white, massive; mud rip-ups	0		Smectite, kaolinite, mica, chlorite
91	1,601.3	Medium-grained sandstone, white, massive; mud rip-ups	0		Smectite, kaolinite, mica, chlorite
90	1,639.5	Mudstone, parallel-laminated, bioturbated	6	R0	Illite-smectite, kaolinite, mica, chlorite
89	1,675	Very fine grained to fine-grained sandstone and siltstone, parallel-laminated, bioturbated	10	R0	Illite-smectite, mica, kaolinite, chlorite, jarosite, albite, calcite, pyrite
88	1,687	Very fine grained to fine-grained sandstone, brown, massive, bioturbated	0		Smectite, kaolinite, mica
87	1,703	Very fine grained to fine-grained sandstone and siltstone, pale-olive, parallel-laminated, bioturbated	0		Smectite, kaolinite, mica
86	1,728	Very fine grained to fine-grained sandstone and siltstone, pale-olive, parallel-laminated, bioturbated	0		Smectite, kaolinite, mica

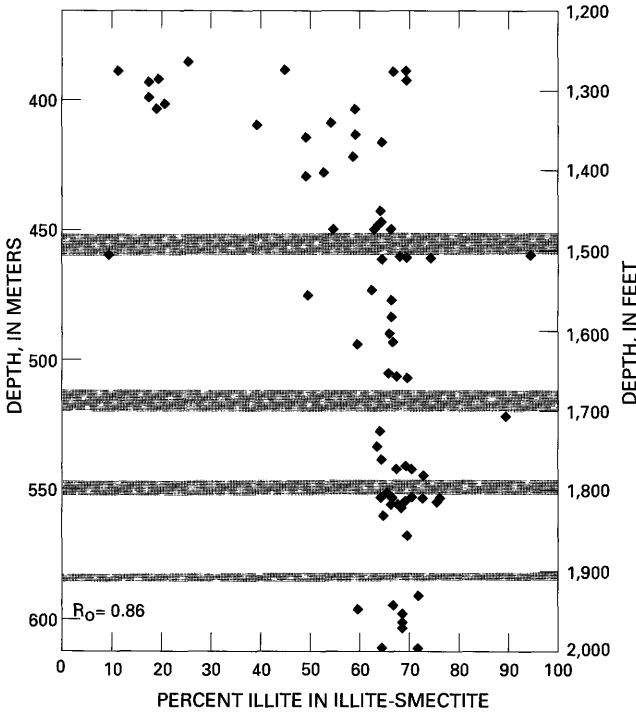


**Figure 8.** Observed expandability of illite-smectite (diamonds) in relation to intrusive rocks (shaded areas), core WC-83-6. Illite-smectite expandabilities were calculated using the  $\Delta 2\theta$  peak positions described in figure 4. Vitrinite reflectance value ( $R_0$ , in percent) is shown for carbonaceous material analyzed.

**Table 4.** Mean vitrinite reflectance values for samples from cores WC-83-5, WC-83-6, and WC-83-17, Washington. [Location of core holes shown in figure 1]

Core	Depth	Mean vitrinite reflectance (percent)
WC-83-5	548.64 m (1,800 ft)	1.69
WC-83-5	534.26 m (1,720 ft)	1.34
WC-83-5	440.74 m (1,446 ft)	1.09
WC-83-5	170.69 m (560 ft)	0.96
WC-83-6	593.75 m (1,948 ft)	0.86
WC-83-17	509 m (1,670 ft)	0.35
WC-83-17	438.91 m (1,440 ft)	0.38
WC-83-17	273.41 m (897 ft)	0.25

Jaeger (1964) reduced the triple integral of heating by diffusion to the more manageable one-dimensional form,

$$T = T_0 [\phi(\epsilon, \tau)], \quad (1)$$

where

$$\phi(\epsilon, \tau) = \frac{1}{2} \left( \operatorname{erf} \frac{\epsilon + 1}{2\sqrt{\tau}} - \operatorname{erf} \frac{\epsilon - 1}{2\sqrt{\tau}} \right). \quad (2)$$

Equations 1 and 2 can be combined to calculate the temperature at a specified distance from an intrusive sheet under deep cover,

**Table 5.** Mathematical relationships for heat-flow calculations.

$T$  = Time-dependent temperature at any given point.

$T_0$  = Initial temperature of magma.

$k$  = Thermal diffusivity of country rock. Values for sedimentary rocks range from 0.004 to 0.012  $\text{cm}^2/\text{sec}$  and for igneous rocks from 0.004 to 0.012  $\text{cm}^2/\text{sec}$ ; this study assumes 0.01  $\text{cm}^2/\text{sec}$ .

$d$  = Half-thickness of the intrusion.

$t$  = Time since intrusion.

$x$  = Distance from midplane of intrusion.

$\tau$  = Dimensionless time, where

$$\tau = \frac{kt}{d^2}$$

$\epsilon$  = Proportional distance from the intrusion, where

$$\epsilon = \frac{x}{d}$$

$l$  = Distance between the midplanes of the two intrusions.

$$\frac{T}{T_0} = \phi(\epsilon, \tau) = \frac{1}{2} \left( \operatorname{erf} \frac{\epsilon + 1}{2\sqrt{\tau}} - \operatorname{erf} \frac{\epsilon - 1}{2\sqrt{\tau}} \right). \quad (3)$$

The temperature at a point  $x$  between two intrusive bodies is simply the combined effect of the two heat sources,

$$\frac{T}{T_0} = \phi(\epsilon_1, \tau_1) + \phi(\epsilon_2, \tau_2), \quad (4)$$

where  $(\epsilon_1, \tau_1)$  are dimensions and conductivities of the first sheet,  $(\epsilon_2, \tau_2)$  are those of the second, and  $(d_2)$  is the thickness of the second, defined as follows:

$$\epsilon_2 = (l - x) / d_2 \quad (5)$$

$$\tau_2 = \frac{kt}{d_2^2}. \quad (6)$$

Using the estimations or measurements for the variables listed in table 6, the time-dependent temperature ( $T$ ) can be calculated for a specified distance or range of distances from the intrusion.

Uncertainty in the original temperature of the intrusion is potentially a source of error. The crystallization of minerals from a magma is an exothermic reaction releasing significant quantities of heat (Jaeger, 1964). This latent heat of crystallization increases the heat flow from the intrusions above that expected for an intrusion undergoing simple cooling without crystallization. The thermal effects of the

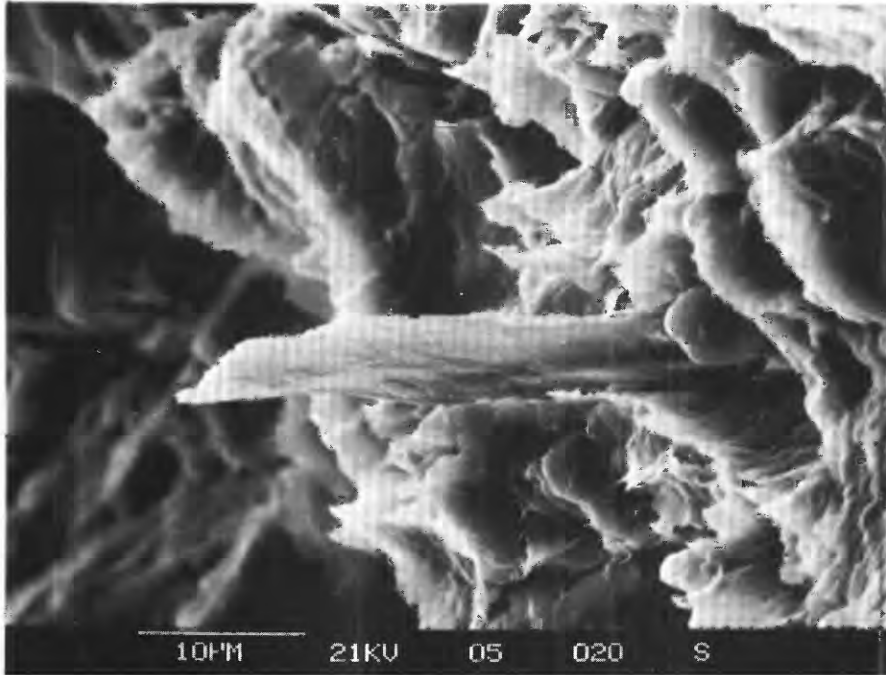


**Figure 9.** Scanning electron micrograph showing typical morphology of illite-smectite. Core WC-83-6, sample 19, depth 1,953 ft (595 m).

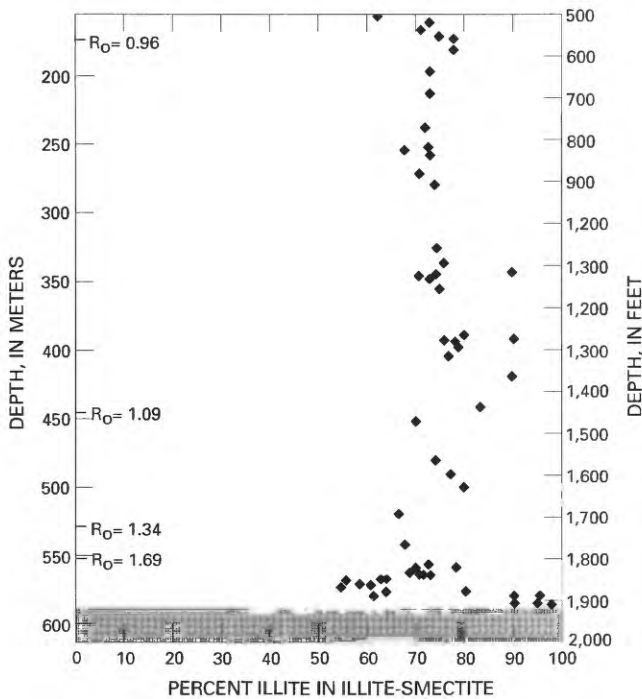


**Figure 10.** Observed expandability of illite-smectite (diamonds) in relation to intrusive rocks (shaded areas), core WC-83-5. Illite-smectite expandabilities were calculated using the  $\Delta 2\theta$  peak positions described in figure 4. Vitrinite reflectance ( $R_0$ , in percent) values are shown for carbonaceous material analyzed.

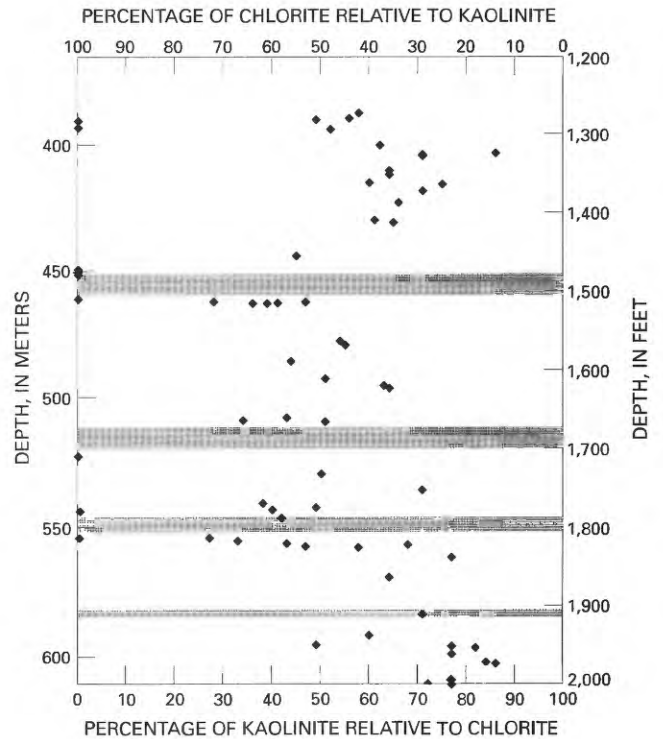


**Figure 11.** Percentages of kaolinite and chlorite relative to each other in relation to intrusion position in core WC-83-6. Percentages were calculated by measuring peak intensities of both kaolinite and chlorite and calculating the ratio of individual peak intensity to the combined peak intensity.

**Table 6.** Values for variables used in heat-flow calculations.

Independent variable	Value	Source
Thermal diffusivity ( $k$ )	0.01 cm <sup>2</sup> /sec	Jaeger (1968).
Initial temperature ( $T_0$ )	900°C–1,200°C	Estimates from igneous petrology.
Time since intrusion ( $t$ )	0.01–100 years	Estimates based on initial calculations from intrusion thicknesses.
Intrusion thickness ( $d$ )	2.6–9.75 m (8.5–32 ft)	Measured in core.
Distance from intrusion ( $x$ )	0.03–57.3 m (0.1–188 ft)	Measured in core.
Distance between intrusions ( $l$ )	32.3–63.4 m (106–208 ft)	Measured in core.

latent heat of crystallization can be simulated by artificially raising the initial temperature of the intrusions. In addition, the presence of water in the melting process reduces the magma temperature. Depression of the dry melting temperature of basalt by water was probably offset by the temperature increase attributed to the latent heat of crystallization. In these samples it was impossible to determine a more precise estimation of water content using the petrographic descriptions, and thus it was difficult to estimate intrusion temperatures. A range of probable intrusion temperatures of 900°C–1,200°C was used for the heat-flow calculations.

The calculations were performed on a Macintosh computer using spreadsheets developed in Microsoft Excel. Individual spreadsheets were used to calculate the temperature at various times and distances between intrusions of the core. Temperature distributions were calculated in log years (0.01, 0.1, 1, 10, and 100 years) because heat flow is time dependent. Heating beyond 100 years was not calculated because cooling from intrusions of this thickness is essentially complete within 100 years. Temperature distributions are expressed as the ratio of the initial intrusion temperature to the temperature after each time increment. For graphing purposes this temperature ratio was converted to actual temperature based on assumed intrusion temperatures.

The temperature of the host rock near the intrusions was calculated for each sample and plotted in relation to depth (figs. 14–17). Figure 14 illustrates the calculated temperature distribution between two intrusions in core WC–83–6. The temperature distribution between all the parallel intrusions of core WC–83–6 is shown in figure 15. Calculating the temperature distribution related to the

intrusion in core WC–83–5 is somewhat less complex because there is only one intrusion and thus no additive heating from other intrusions. Although the calculations for the single intrusion of core WC–83–5 are less complex, the calculated temperature distribution has much more uncertainty because of the unknown thickness of the intrusion at the bottom of the core. Two temperature distributions were calculated. In one distribution (fig. 16), we assumed that the intrusion ends just slightly beyond the end of the core, making the intrusion 26 m (85 ft) thick; in the second (fig. 17), we assumed that the intrusion is 61 m (200 ft) thick.

## DISCUSSION

### REACTION KINETICS

Prior to reaching equilibrium, the rate at which a chemical reaction proceeds can be expressed in terms of temperature, time, and concentration of reactants. Based on the hard-shell theory of reaction kinetics, a fundamental chemical reaction requires the collision of two molecules, and the reaction rate must be proportional to the frequency of collisions (Laidler and Meiser, 1982). The frequency factor is a measure of the number of times per second that atoms are close enough to react. For a reaction to occur between stable molecules, a certain amount of energy, termed “activation energy,” must be absorbed to weaken the bonds holding the reactant molecules together. Complex mineral reactions such as the illitization reaction consist of numerous fundamental chemical reactions proceeding along parallel and (or) sequential paths. Nevertheless, the overall reaction can be

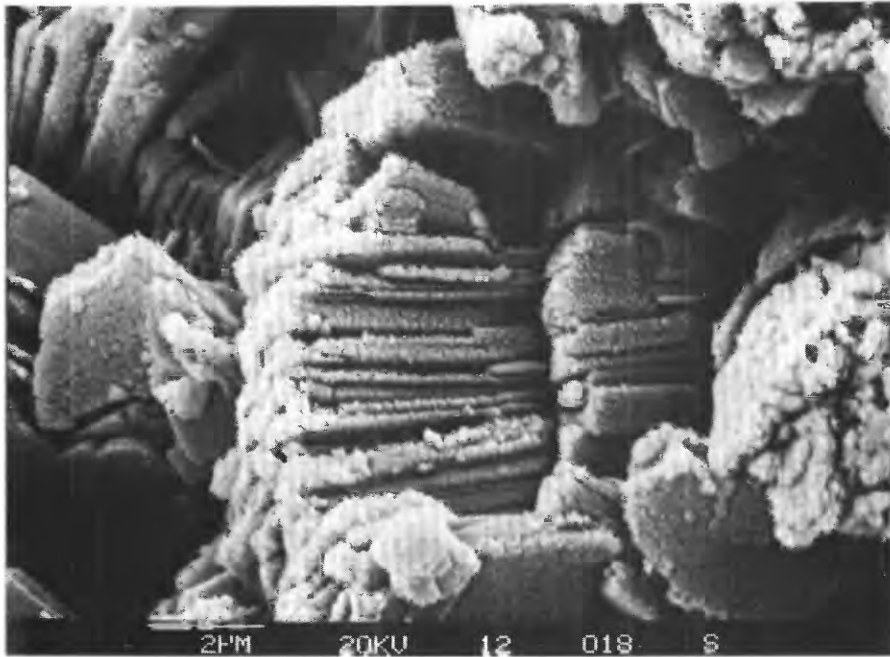


**Figure 12.** Scanning electron micrograph of kaolinite. Core WC-83-6, sample 79, depth 1,283 ft (391 m).

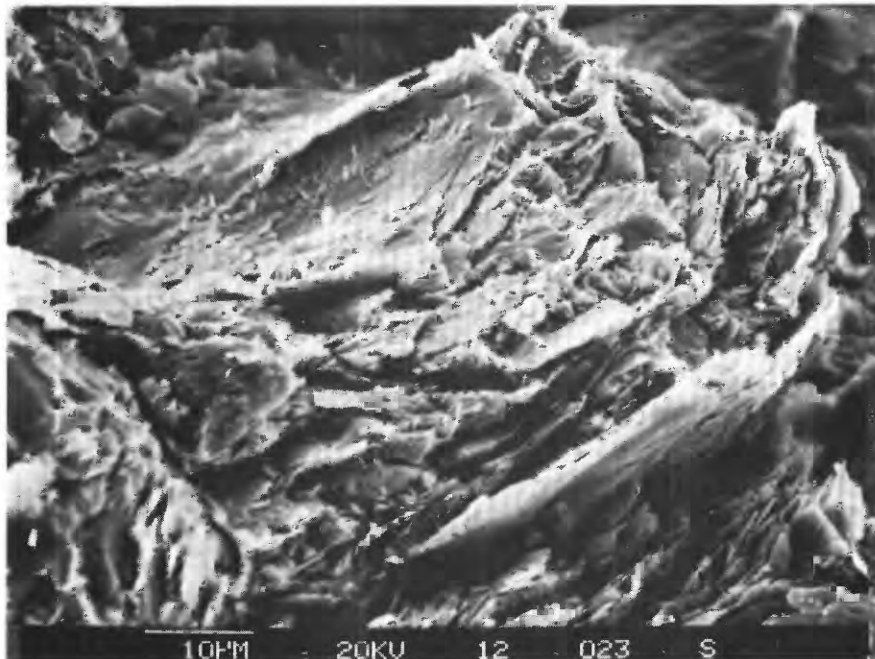


**Figure 13.** Scanning electron micrograph of chlorite replacing biotite. Core WC-83-6, sample 73, depth 1,318.8 ft (402 m).

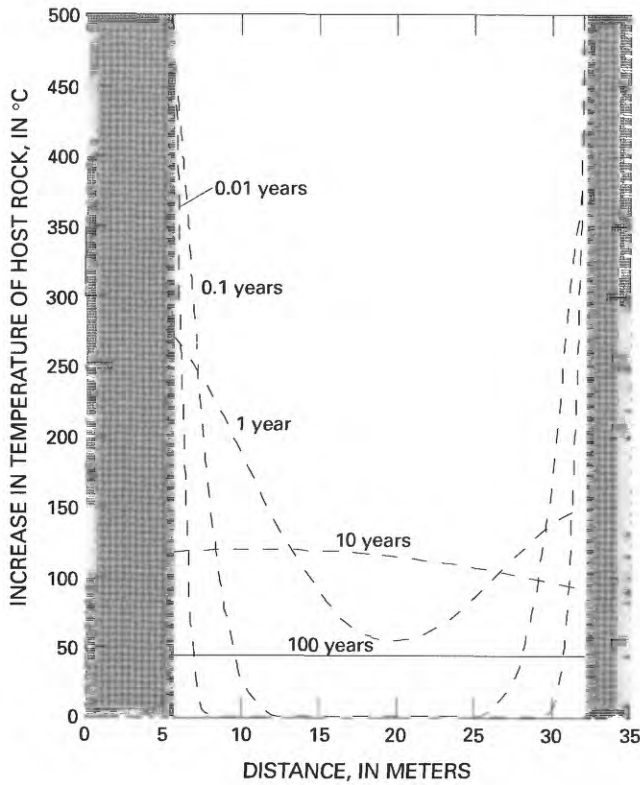


**Figure 14.** Calculated temperature between two intrusions (shaded) 6 m and 3 m (19.5 and 10 ft) thick at various times after emplacement. Intrusion temperature is assumed to be 1,000°C. Midpoints of the two intrusions are 32.3 m (106 ft) apart.

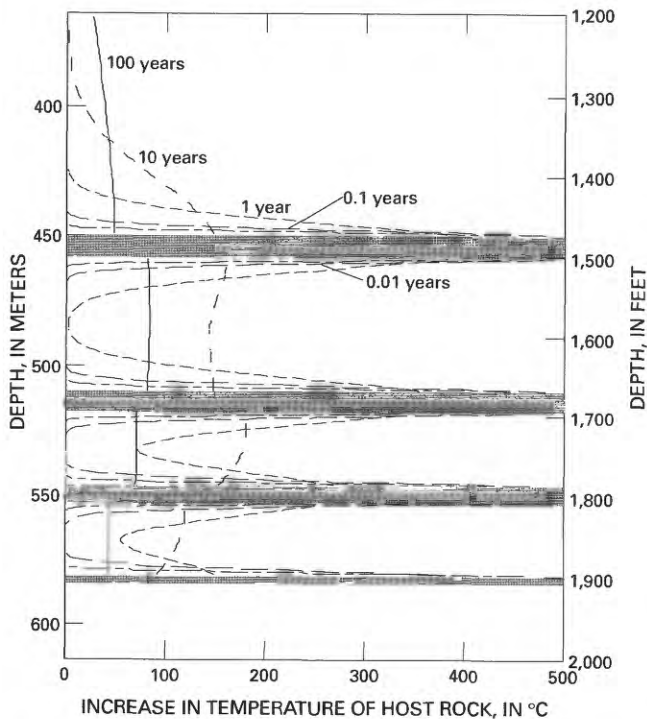


**Figure 15.** Calculated temperature between intrusions (shaded) in core WC-83-6 at various times after the simultaneous emplacement of the intrusions. Intrusion temperature is assumed to be 1,000°C.

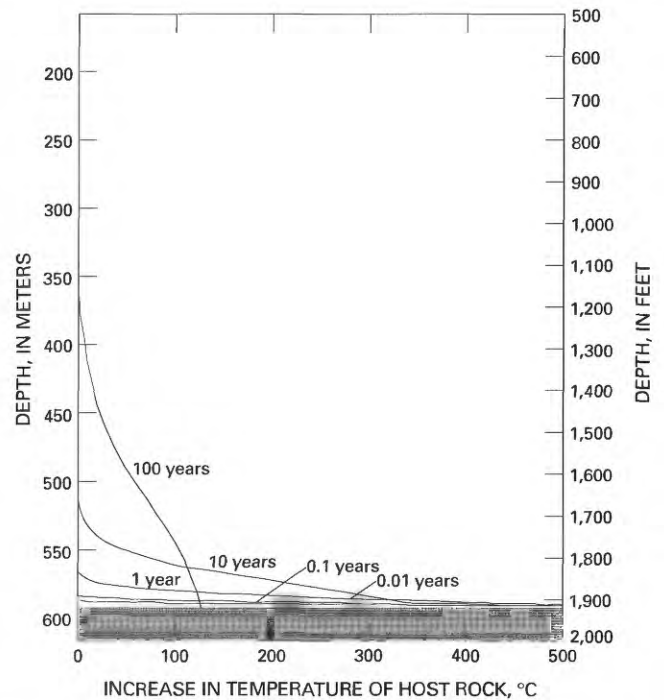


**Figure 16.** Calculated temperature at various times after emplacement of a 26-m-thick (85 ft) intrusion (shaded) in core WC-83-5. Intrusion temperature is assumed to be 1,000°C. A 26-m-thick intrusion assumes that the intrusion terminates just beyond the bottom of the retrieved drill core.

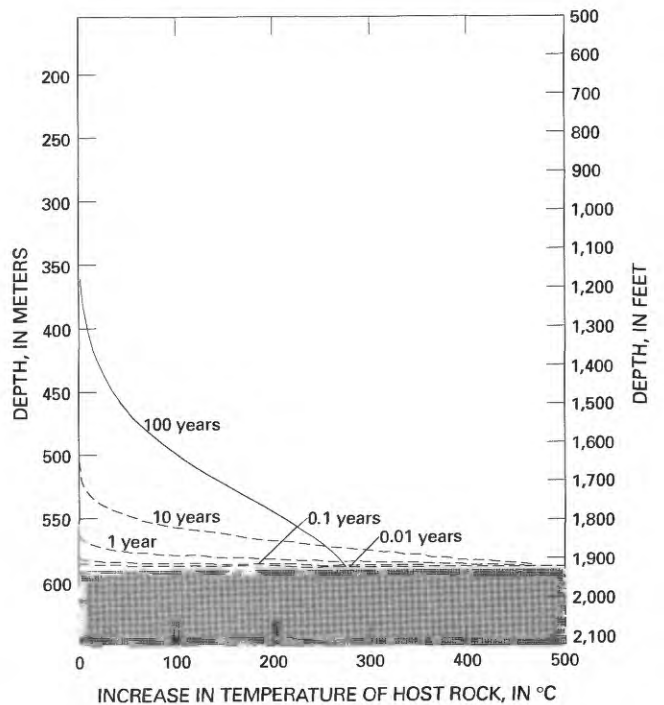


**Figure 17.** Calculated temperature at incremental times after emplacement of a 61-m-thick (200 ft) intrusion (shaded) in core WC-83-5. Intrusion temperature is assumed to be 1,000°C. A 61-m-thick intrusion assumes a much thicker intrusion than that shown in figure 16, one that does not terminate just beyond the bottom of the retrieved drill core but has a similar sheetlike geometry.

expressed in terms of a single simplified kinetic expression using a single activation energy and a single pre-exponential function.

For example, the reaction of smectite to illite, expressed as a first-order reaction, would obey the equation,

$$-\frac{dS}{dt} = kS_0 \quad (7)$$

where

- $S_0$  = Initial percentage of smectite layers
- $k$  = First-order rate constant (reciprocal units of time)
- $t$  = Time
- $dS$  = Incremental change in smectite content
- $dt$  = Incremental change in time.

The effect of temperature on the rate constant ( $k$ ) is expressed in the Arrhenius equation,

$$k = Ae^{-\frac{U}{RT}} \quad (8)$$

where

- $A$  = Pre-exponential function (reciprocal units of time), also called the frequency factor
- $U$  = Activation energy (kJ/mole)
- $R$  = Gas constant = 1.987 cal/K mol or 8.314 J/K mol
- $T$  = Temperature (Kelvin).

The Arrhenius equation may be substituted into the first-order rate law,

$$-\frac{dS}{dt} = S_0 Ae^{-\frac{U}{RT}} \quad (9)$$

Equation 9 relates the progress of a reaction, with respect to time, at a given temperature. In this case  $dS/dt$  is the change in the number of smectite layers in illite-smectite for a given change in time.

This rather simplistic treatment of illitization reaction kinetics is complicated by the fact that a number of researchers have proposed widely divergent values for reaction order, activation energy, and pre-exponential function (table 7). These differences arise from the fact that the reaction involves a chemically diverse and imperfectly characterized group of minerals reacting under a variety of temperature-time-chemistry conditions.

## FACTORS AFFECTING ILLITIZATION REACTION RATES

In general, fluid-rock interactions affect chemical and mineralogical reactions in country rock near intrusions (Kerrick, 1991). Within such an alteration zone, the availability of potassium and chemistry of the fluids can profoundly affect the rate and extent of illitization (Eberl and Hower, 1977; Roberson and Lahann, 1981; Whitney, 1992). Huang and others (1993) suggested that, although magnesium

significantly retards the illitization reaction rate, calcium may not retard the reaction rate as much as previously thought, and sodium retards the reaction rate only in high concentrations. Additionally, the chemical composition of the starting smectite affects illitization reaction rates because in hydrothermal environments trioctahedral (magnesium-rich) smectite and iron-rich smectite react to illite much more slowly than does dioctahedral aluminous smectite (Eberl and others, 1978; Whitney, 1983; Chang and others, 1986; Couto Anjos, 1986). The activity of water in the system is also an important factor in illitization (Whitney, 1990). In fluid-deficient systems (where pore spaces are not saturated), the rate and extent of illitization may be significantly inhibited. Even differences in texture may affect the illitization reaction (Whitney and Velde, 1993). In comparison of massive and laminated shales, Howard (1987) documented increased illitization in laminated shale that he interpreted to be a result of the laminations acting as fluid conduits.

Thus, the lithology, chemical composition, and texture of the rocks into which igneous sills are intruded can influence solution chemistry, water availability, and starting mineralogy, and these variables in turn affect illitization rates and contribute to scatter in the observed data. The lithological inhomogeneity of the rocks in this study results from varying sedimentary facies associated with the fluvial-deltaic depositional environment. In this setting, small-scale variations in bulk chemistry, potassium availability, organic matter, and fluid flow are expected. Each of these small-scale variations can locally affect the illitization reaction rate and contribute to the observed scatter in the data. Despite these uncertainties, it is possible to model the extent of the illitization reaction in response to heating caused by an igneous intrusion in order to test whether the heat from the intrusions accounts for the patterns of illitization observed in the core.

## CALCULATIONS OF THE EXTENT OF THE ILLITIZATION REACTION

As mentioned above, different researchers have reached different conclusions regarding the reaction kinetics of the illitization reaction. Table 7 shows the range of values for the kinetic expressions for the illitization reaction proposed by different authors. Some workers believe that the overall reaction of smectite to illite obeys a first-order rate law with respect to the expandability (percent smectite layers) of the illite-smectite (Eberl and Hower, 1976; McCubbin and Patton, 1981), whereas other researchers have suggested a higher order rate law for the reaction (Pytte, 1982; Whitney and Northrop, 1988; Huang, 1992). The kinetic formulation for illitization used in the present study is based on reaction rates calculated from burial in natural sedimentary basins by Velde and Vasseur (1992). Velde and Vasseur's model uses sequential first-order kinetic formulations that divide the reaction into two stages, the first stage

**Table 7.** Published kinetic values used in the Arrhenius equation for activation energy and pre-exponential function during illitization. [Arrhenius equation is given in text]

Researcher	Activation energy U (kJ/mol)	Setting	Reaction order	Pre-exponential function)
Velde and Vasseur (1992)	R0=69.7	Burial	1	$R0=e^{21.5}/\text{Ma}$
	R1=37.4		1	$R1=e^{7.2}/\text{Ma}$
Eberl and Hower (1976)	82	Laboratory	1	$e^{11.8}/\text{day}$
Howard and Roy (1985)	12.5–14.5	Laboratory	1	$e^{11.8}/\text{day}$
Pytte (1982)	138	Contact metamorphism	6	$e^{49}/\text{second}$
Huang and others (1991, 1993)	117.2	Laboratory	3	$e^{11.3}/\text{second}$
Roberson and Lahann (1981)	125.6	Laboratory	1	$e^{22.5}/\text{day}$

involving the formation of disordered R=0 illite-smectite and the second stage the formation of ordered R=1 illite-smectite. The two-stage reaction is based on an empirical analysis of illitization in several basins having different ages, rates of subsidence, and geothermal gradients. This two-stage kinetic model gives a relatively good estimation of illite-smectite expandability for a wide variety of sedimentary conditions. Separate rate constants are provided for each stage of the sequential formation of the R=0 and R=1 phases, which combine to produce the total reaction extent. Using this kinetic approach, the final expandability can be calculated based on specific time (age) and temperature (maximum depth of burial and the geothermal gradient) conditions.

We attempted to simulate the observed illitization reaction profiles in the intruded sedimentary rocks by combining the thermal profiles calculated using the equations of Jaeger (1964) and the kinetic expressions developed by Velde and Vasseur (1992). As a first attempt, the calculations were made using only heat from the intrusions and no other heat sources. Assuming pure smectite as a starting material, kinetic variables (activation energy and pre-exponential function) can be selected such that the calculated illitization matches the measured maximum illitization adjacent to the intrusions but does not accurately simulate the expandability of illite-smectite farther away from the intrusions; even at small distances from the intrusions the reaction would not proceed at all (no illite in illite-smectite) (fig. 18A). Conversely, if kinetic variables are selected that match the observed illitization midway between the intrusions, the reaction would proceed to completion in huge haloes extending far from the intrusions (100 percent illite in illite-smectite) (fig. 18B). The only way to make the calculated reaction extent profiles match the observed data exactly, using only heat from the intrusions, is to choose unique activation energies and pre-exponential functions for each sample, which is chemically unreasonable.

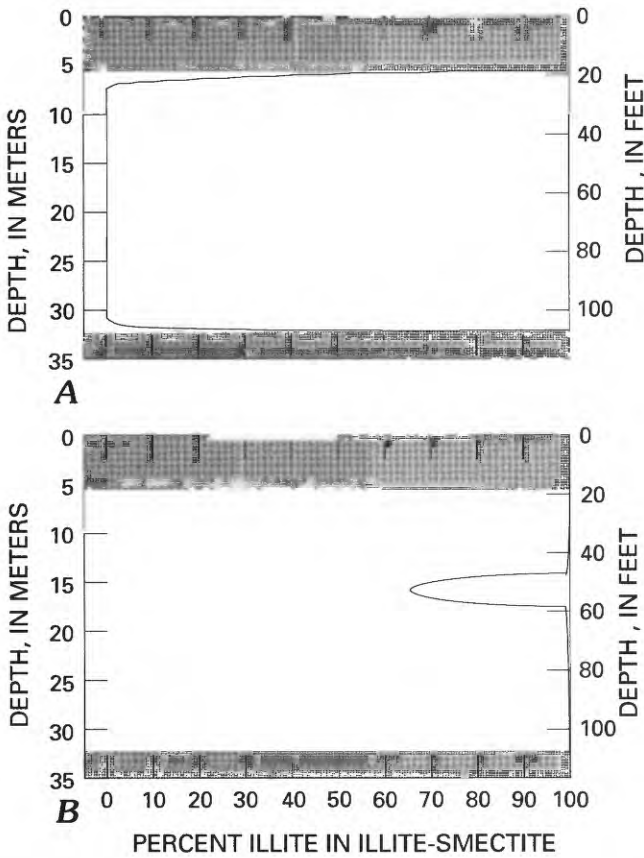
A geologically more reasonable approach to matching the observed expandability profile is to assume a starting mineralogy consisting of illite-smectite containing about 50–70 percent illite layers. There are two possible ways to

get this starting material: (1) detrital illite-smectite may have been initially 50–70 percent illite in illite-smectite, or (2) the starting material was initially 100 percent expandable, and another source of heat (burial diagenesis?) drove the illitization reaction to about 50–70 percent illite prior to emplacement of the intrusions. Scanning electron microscopy of samples far away from the intrusions shows delicate illite-smectite textures that indicate authigenic formation, not detrital deposition (fig. 9). This textural evidence suggests that the sediments were affected by heating due to burial in addition to heating by the intercalation of the intrusions. Thus, to model realistically the combined extent of illitization in the basin, an estimate of illitization caused by burial must be included.

The extent of illitization produced by burial can be calculated using estimated depths of burial and geothermal gradients. Stratigraphic reconstruction of measured field sections suggests a minimum depth of burial of 3 km (Fisher, 1957). A slightly elevated geothermal gradient of about 35°C/km is based on organic thermal maturity profiles (Walsh and Lingley, 1991). The extent of the illitization reaction produced by heat derived from burial constitutes a baseline for calculating the extent of the reaction resulting from heating by the intrusions. The straight lines in figures 19–22 reflect the calculated extent of illitization in core WC–83–6, based on 3.3 km of burial and a geothermal gradient of 35°C/km. The straight lines in figures 23–30 show the calculated extent of illitization in core WC–83–5, based on a similar geothermal gradient and slightly deeper (4.1 km) burial. All estimates of burial diagenesis assume a depositional age of 40 million years for these Eocene sedimentary rocks. Calculations used to estimate the expected extent of illitization resulting from burial are based on published values of rate parameters for burial environments (Velde and Vasseur, 1992). The first stage of the reaction (R=0) is modeled using an activation energy of 69.7 kJ/mol and a pre-exponential factor of  $e^{21.5}/\text{Ma}$ . The second stage of the reaction (R=1) is modeled using an activation energy of 37.4 kJ/mol and a pre-exponential factor of  $e^{7.2}/\text{Ma}$ .

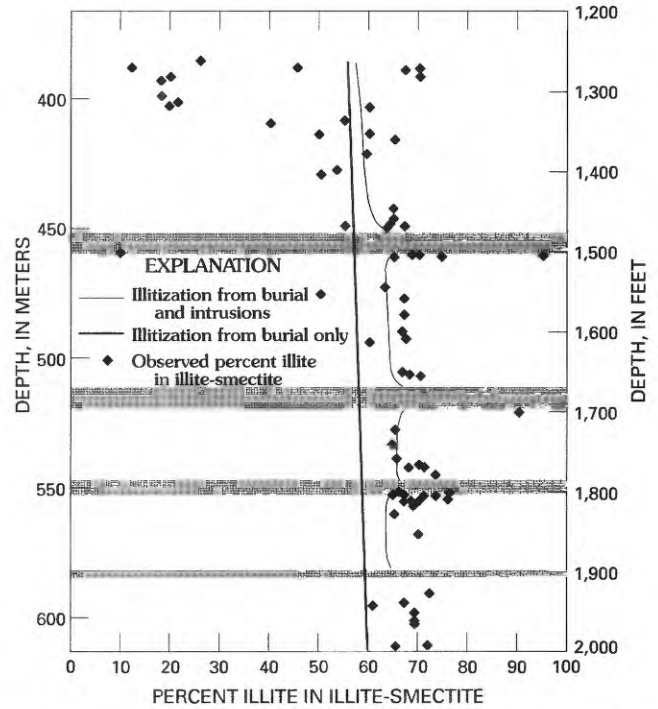
The increase in illitization caused by heat from intrusion was estimated using the temperature-time distributions

calculated in the previous section. The kinetic model used for burial was also used to calculate the increase in illitization due solely to intrusions. Activation energies employed to calculate reaction extent were identical to those used for burial calculations,  $R_0=69.7$  kJ/mol and  $R_1=37.4$  kJ/mol (Velde and Vasseur, 1992). Figures 19–30 show the calculated total reaction extent due to the combined effect of heat provided by burial and by intrusion for a range of intrusion temperatures from 900°C to 1,200°C. Because the true thickness of the intrusion in core WC-83-5 is unknown, figures 23–30 show illitization for a temperature range of 900°C–1,200°C for two

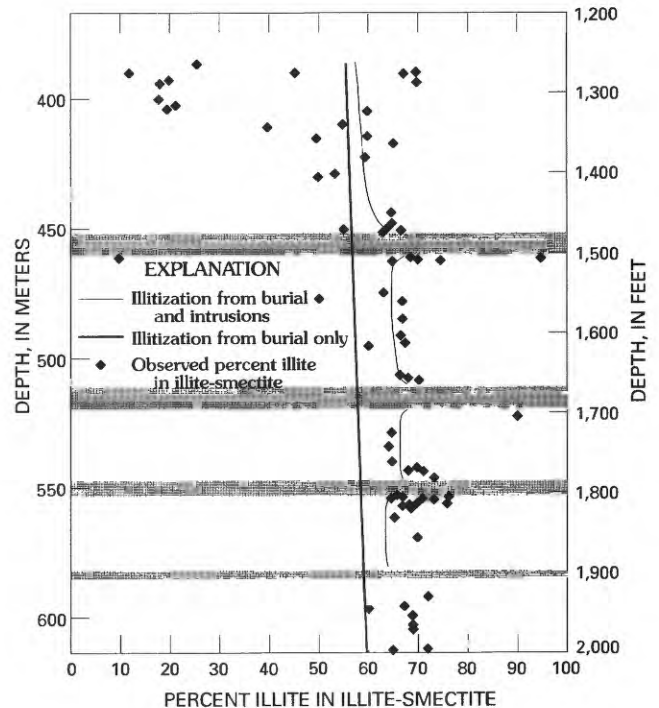


**Figure 18.** Calculated illitization reaction extent using only heat provided by the intrusions (shaded). Using only the heat provided by the intrusions in a single reaction model, the illitization reaction can be modeled either (A) to fit the observed illitization near the intrusions or (B) to fit the observed illitization at the midpoint between the intrusions, but not both.

**Figure 20 (facing column).** Comparison of calculated and observed percent illite in illite-smectite for core WC-83-6 using 1,000°C intrusions (shaded) for calculations. Illitization from burial only assumes burial depth of 3 km, geothermal gradient of 35°C/km, and depositional age of 40 million years.



**Figure 19.** Comparison of calculated and observed percent illite in illite-smectite for core WC-83-6, using 900°C intrusions (shaded) for calculations. Illitization from burial only assumes burial of 3 km, geothermal gradient of 35°C/km, and depositional age of 40 million years.



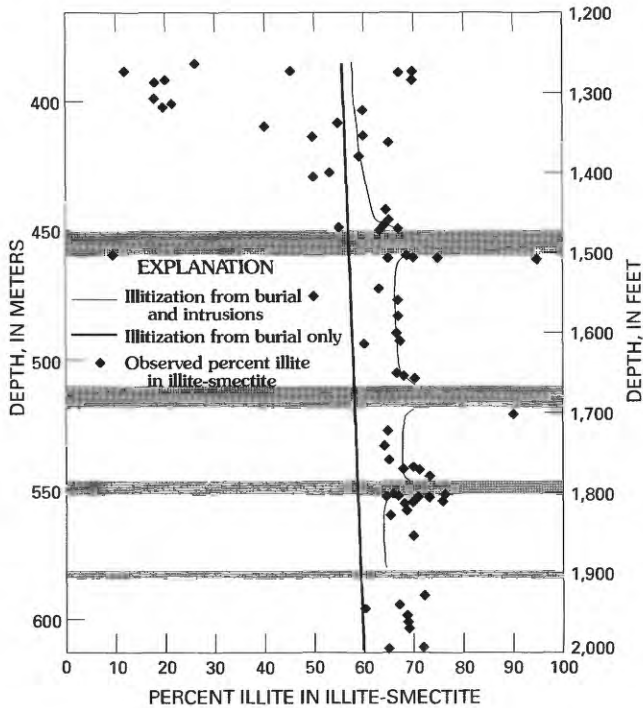


**Figure 21.** Comparison of calculated and observed percent illite in illite-smectite for core WC-83-6 using 1,100°C intrusions (shaded) for calculations. Illitization from burial of 3 km, geothermal gradient of 35°C/km, and depositional age of 40 million years.

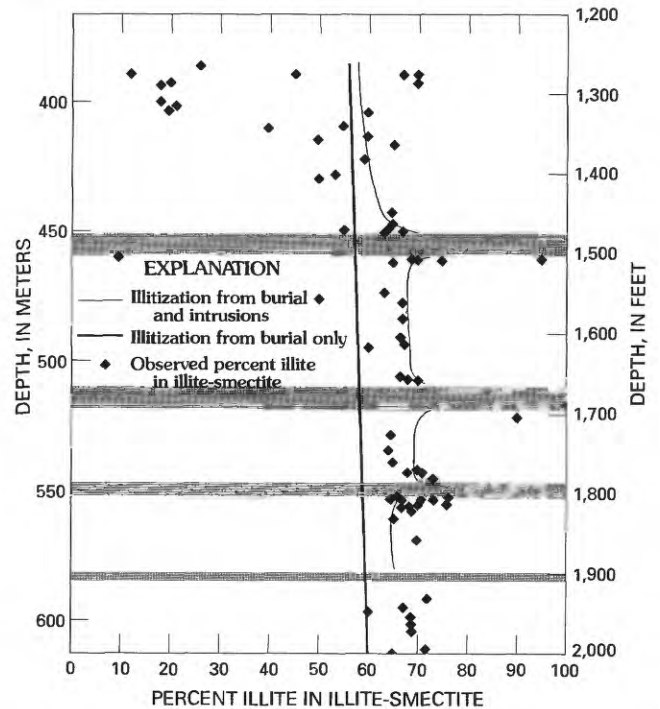


**Figure 22.** Comparison of calculated and observed percent illite in illite-smectite for core WC-83-6 using 1,200°C intrusions (shaded) for calculations. Illitization from burial only assumes burial depth of 3 km, geothermal gradient of 35°C/km, and depositional age of 40 million years.

thicknesses. Superimposed on the calculated curves are the observed values of illitization (from tables 1 and 2) of core samples.

Although the same activation energy values were used in both burial and intrusive heating scenarios, satisfactory curves could not be calculated unless the pre-exponential function was changed. According to these calculations, the illitization reaction would not proceed adjacent to the intrusions if pre-exponential functions used for the burial setting were applied to the intrusive heating situation. The pre-exponential value used for burial diagenesis is based on low temperatures and long times. A higher value is appropriate for contact metamorphism during which temperatures are much higher for shorter periods (Lasaga, 1981). Therefore, pre-exponential factors were adjusted on a trial and error basis until observed illite-smectite expandabilities were matched by the calculated curves. The pre-exponential factor for the second ( $R=1$ ) stage of the kinetic calculation was adjusted upward from  $4.24 \times 10^{-11}/\text{sec}$  to  $2.12 \times 10^{-6}/\text{sec}$  for the multiple intrusions of core WC-83-6 and to  $2.12 \times 10^{-7}$  for core WC-83-5. These pre-exponential factors are about halfway between the values used in the burial model above and experimentally determined estimates for short-duration heating events of about 1.5 per second (Eberl and Hower, 1976). Because the pre-exponential factor is a

temperature-dependent function based on molecular collision frequency, the higher values of pre-exponential factor chosen for these calculations are justified (Lasaga, 1981). The first stage ( $R=0$ ) of the reaction was not adjusted similarly because that part of the reaction had mostly gone to completion as a result of burial alone. Table 8 summarizes the kinetic values used to calculate expected illitization reaction extent.

The calculated models of reaction extent for the two intruded cores, including both burial and intrusive heat (figs. 19–30), fit the observed data reasonably well. In the case of four parallel intrusions (core WC-83-6), the calculated expandabilities compare well with the observed data especially at higher intrusive temperatures (figs. 21, 22, 1,100°C–1,200°C) and below a depth of 457.2 m (1,500 ft). The simulations match the data much better for the section of the core between the intrusions at a depth of 457.2–579.1 m (1,500–1,900 ft) than for the shallower part of the well, for which the observed illitization is significantly less than the predictions. The reason for these unexpectedly high expandabilities at about 396.2 m (1,300 ft) is not clear. It may be possible to explain this anomaly using something as simple as a change in sediment source. Alternately, very thin extrusive bodies (labeled as flows in fig. 6) may have been releasing

**Table 8.** Kinetic values used for activation energy and pre-exponential function to calculate illitization.

Setting	Activation energy $U$ (kJ/mol)	Reaction order	Pre-exponential function $A$
Burial (Velde and Vasseur, 1992)	$R0=69.7$	1	$R0=e^{21.5/Ma}$
	$R1=37.4$	1	$R1=e^{7.2/Ma}$
Intrusions (core WC-83-5)	$R0=69.7$	1	$R0=e^{21.5/Ma}$
	$R1=37.4$	1	$R1=e^{18/Ma}$
Intrusions (core WC-83-6)	$R0=69.7$	1	$R0=e^{21.5/Ma}$
	$R1=37.4$	1	$R1=e^{15.7/Ma}$

magnesium, iron, and calcium from unstable mafic grains and locally saturating the surrounding sediments and inhibiting the burial illitization reaction. The only other very highly expandable sample (sample 57, 458.4 m (1,504 ft)) in this core also is within 1 m of another flow.

The large intrusion at the bottom of core WC-83-5 is modeled best by a 61-m-thick (200 ft), 1,000°C intrusion (fig. 28). The anomalously expandable samples at about 579.1 m (1,900 ft) in this core are more difficult to explain because they are closer to the thick intrusion and there are no extrusive rocks nearby, but they may also reflect a change in sediment source. Alternatively, if they represent a continuous sediment source, their anomalous expandability may be an indicator of the timing of the intrusion and the burial. If burial preceded intrusion, the observed illitization would be relatively smooth and continuous (as are the dark lines in figs. 19–30) and would serve as a starting point for illitization due to intrusions (the thin lines in figs. 19–30). If, however, intrusion preceded burial (or occurred after very little burial), illitization would proceed rapidly and almost completely in a narrow zone near the intrusion. Highly expandable illite-smectite (or pure smectite) would remain stable at some distance from the intrusion (similar to fig. 18A). If fluids rich in sodium, calcium, magnesium, and iron were released from the intrusion as it cooled, the fluids would inhibit any subsequent illitization. Although this hypothesis cannot be proven by this study, such a scenario would produce an amount of illitization less than that used as a baseline in an area adjacent to an intrusion where the model otherwise predicts illitization well above the baseline.

### CONDUCTION, DIFFUSION, AND ADVECTION NEAR INTRUSIONS

Near intrusions, heat may be transferred by conduction, or it may accompany the advection of fluids (Ferry and Dipple, 1991). In the case of heat transfer, the model used in this study (Jaeger, 1968) considers host-rock heating resulting purely from conduction. Convective fluid flow near igneous intrusions may redistribute the heat in the country rock but does little to affect the rate of heat transfer

from the intrusion (Furlong and others, 1991). Thus, if fluid movement carried heat away from the intrusion, the temperature gradients might not be as steep as indicated in figures 14–17, although the duration of heating would be similar. Stable-isotope techniques have been used to study conduction-dominated contact metamorphic systems around large plutons (Sheih and Taylor, 1969), and unless there is strong evidence to suggest otherwise it is best to assume that conductive heat transfer dominates (Furlong and others, 1991). In the present study, the narrow thermal alteration zone adjacent to the intrusions and the lack of textural evidence for fluid movement in the sediments near the intrusion suggest that advective effects were minimal.

### PARAGENESIS OF OTHER MINERALS

The formation of authigenic carbonate minerals (calcite, dolomite, and siderite) in rocks near the intrusions implies that calcium, magnesium, and iron were mobile, at least over short distances. Whether these ions came from fluids released by the cooling intrusions or from dissolution of framework grains is unclear, but their presence may have locally inhibited the illitization reaction as described previously. Additionally, the presence of authigenic albite in the <1- $\mu$ m size fraction indicates that sodium is abundant throughout most of the core. In contact metamorphic environments containing abundant sodium, the conversion of mafic minerals to chlorite is very common (Barton and others, 1992). Petrographic data show that chlorite formed predominantly as replacement of mafic minerals, not as pervasive pore filling or grain coatings. Formation of chlorite may have predated the formation of illite-smectite, or chlorite may have precipitated contemporaneously with the illite-smectite during intrusive heating. The general increase in chlorite abundance near the intrusions suggests that it is a byproduct of the heating from the intrusions. Likewise, the depletion of kaolinite near the intrusions suggests that kaolinite predated the intrusions and was destroyed during the contact metamorphic processes when the intrusions were emplaced.

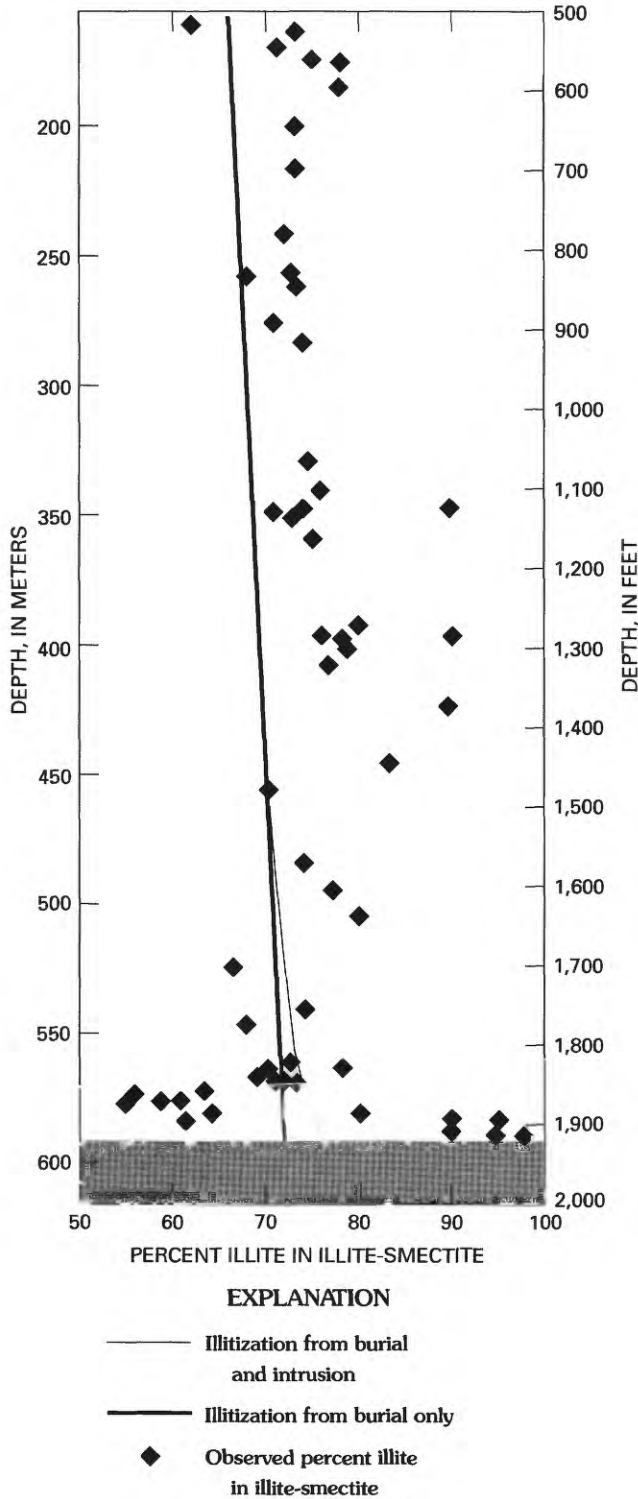


**Figure 23.** Comparison of calculated and observed percent illite in illite-smectite for core WC-83-5 using a 26-m-thick (85 ft), 900°C intrusion (shaded) for calculations. Illitization from burial only assumes burial depth of 4.1 km, geothermal gradient of 35°C/km, and depositional age of 40 million years.

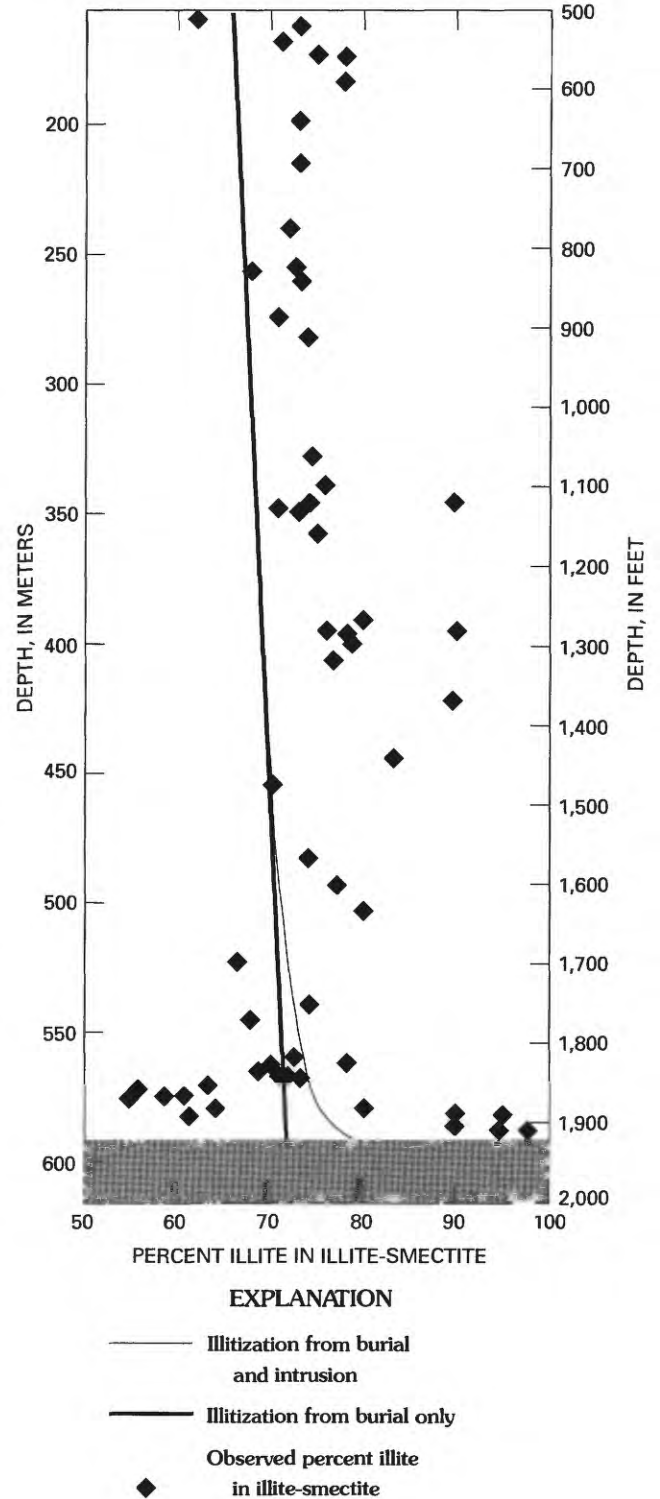


**Figure 24.** Comparison of calculated and observed percent illite in illite-smectite for core WC-83-5 using a 26-m-thick (85 ft), 1000°C intrusion (shaded) for calculations. Illitization from burial only assumes burial depth of 4.1 km, geothermal gradient of 35°C/km, and depositional age of 40 million years.

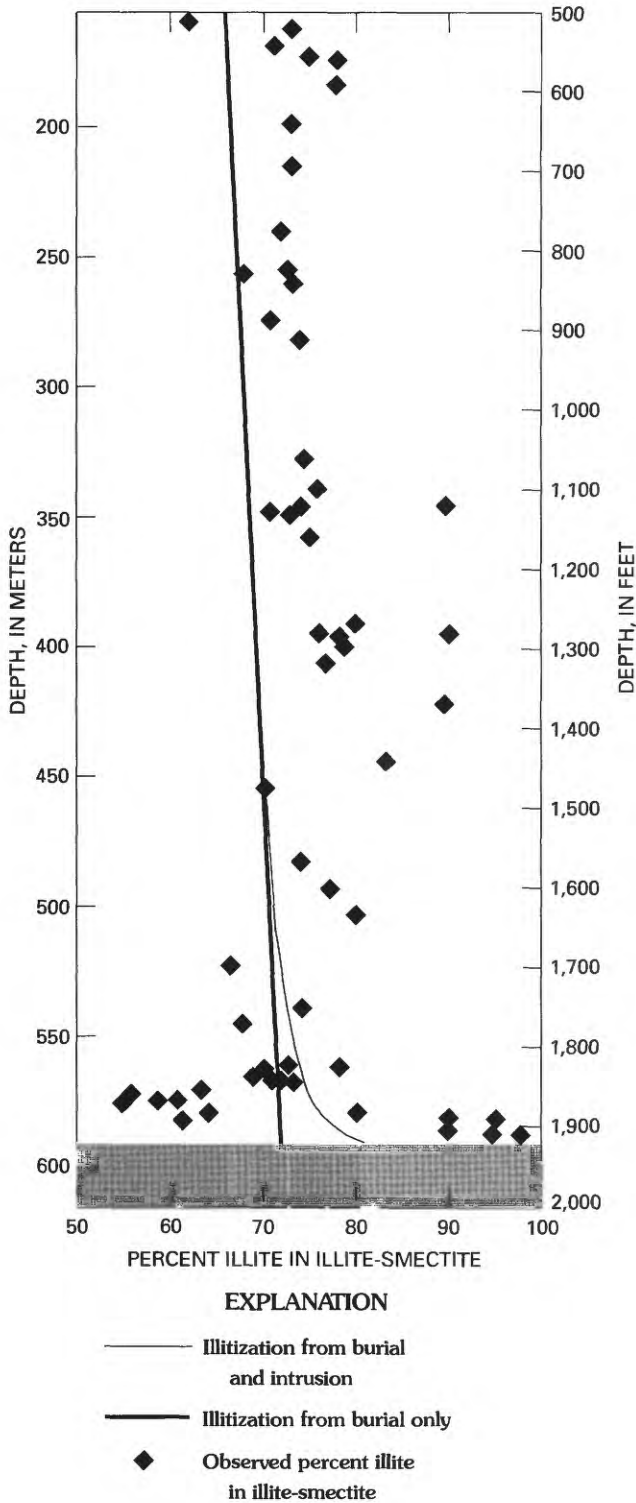


**Figure 25.** Comparison of calculated and observed percent illite in illite-smectite for core WC-83-5 using a 26-m-thick (85 ft), 1,100°C intrusion (shaded) for calculations. Illitization from burial only assumes burial depth of 4.1 km, geothermal gradient of 35°C/km, and depositional age of 40 million years.

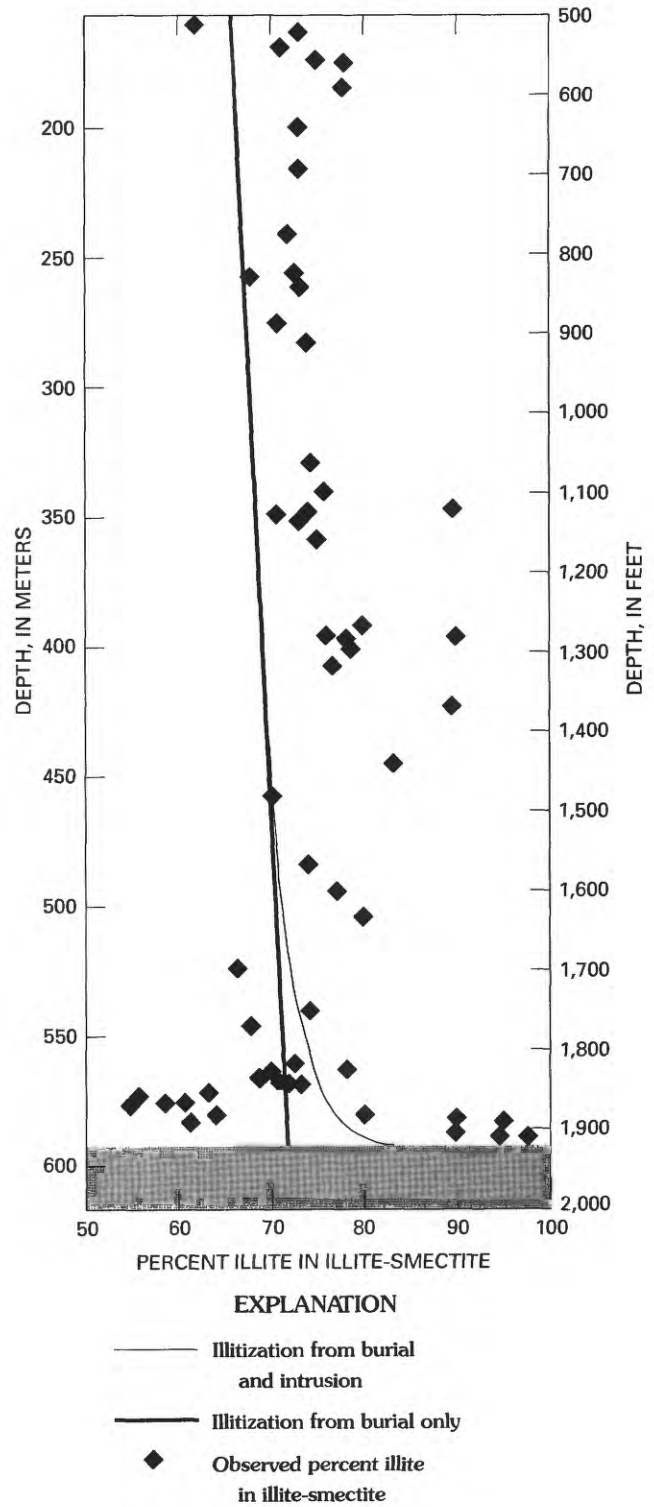


**Figure 26.** Comparison of calculated and observed percent illite in illite-smectite for core WC-83-5 using a 26-m-thick (85 ft), 1,200°C intrusion (shaded) for calculations. Illitization from burial only assumes burial depth of 4.1 km, geothermal gradient of 35°C/km, and depositional age of 40 million years.

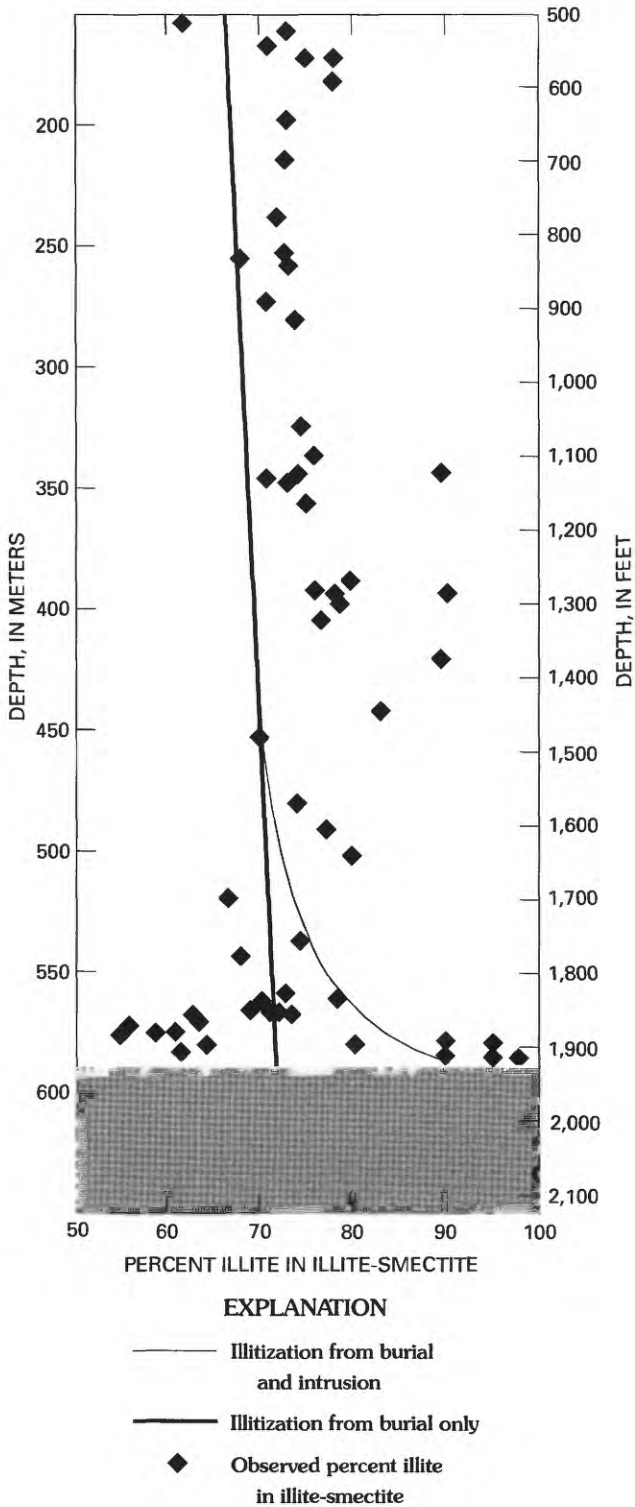


**Figure 27.** Comparison of calculated and observed percent illite in illite-smectite for core WC-83-5 using a 61-m-thick (200 ft), 900°C intrusion (shaded) for calculations. Illitization from burial only assumes burial depth of 4.1 km, geothermal gradient of 35°C/km, and depositional age of 40 million years.

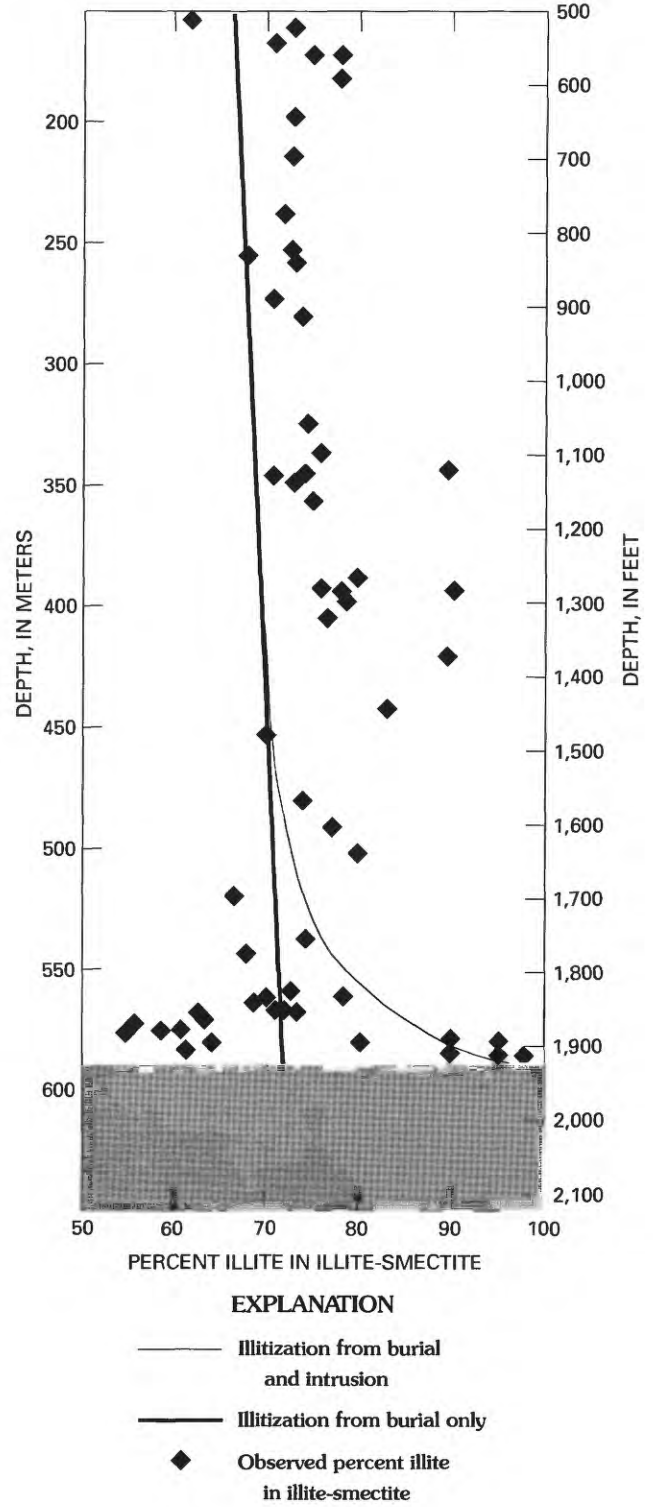


**Figure 28.** Comparison of calculated and observed percent illite in illite-smectite for core WC-83-5 using a 61-m-thick (200 ft), 1,000°C intrusion (shaded) for calculations. Illitization from burial only assumes burial depth of 4.1 km, geothermal gradient of 35°C/km, and depositional age of 40 million years.

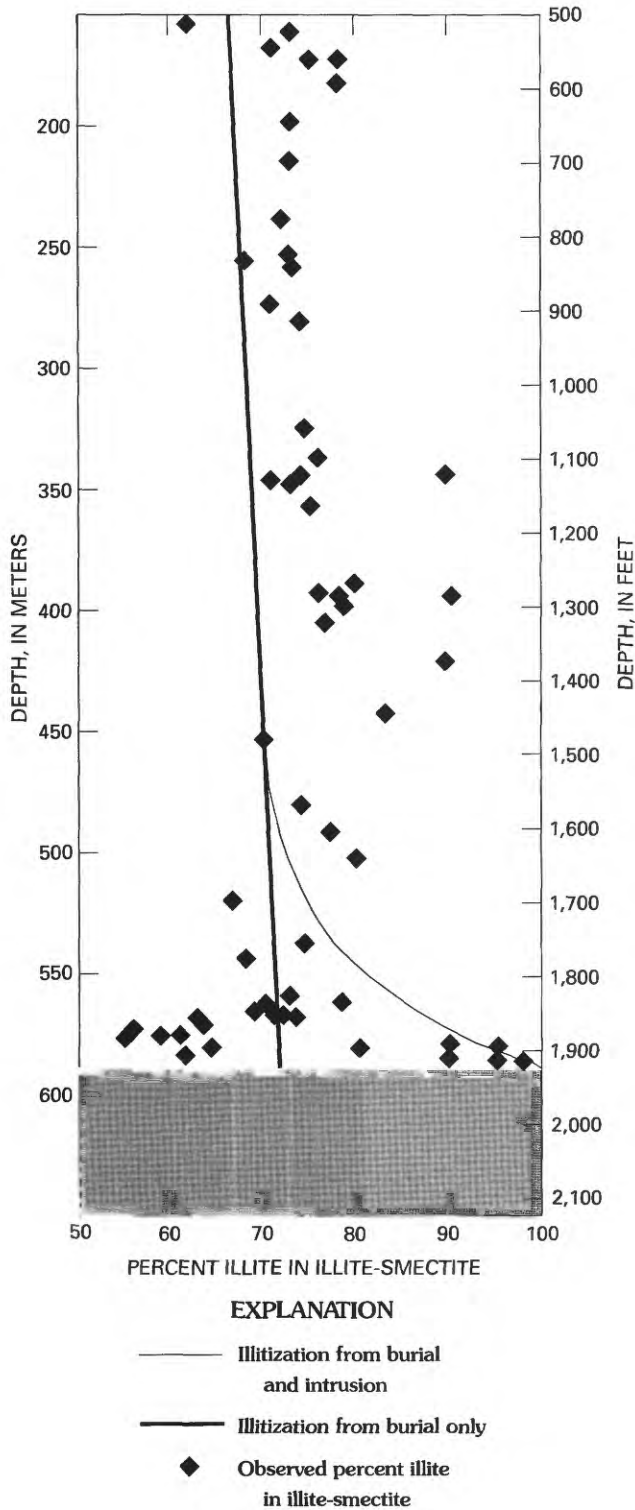


**Figure 29.** Comparison of calculated and observed percent illite in illite-smectite for core WC-83-5 using a 61-m-thick (200 ft), 1,100°C intrusion (shaded) for calculations. Illitization from burial only assumes burial depth of 4.1 km, geothermal gradient of 35°C/km, and depositional age of 40 million years.

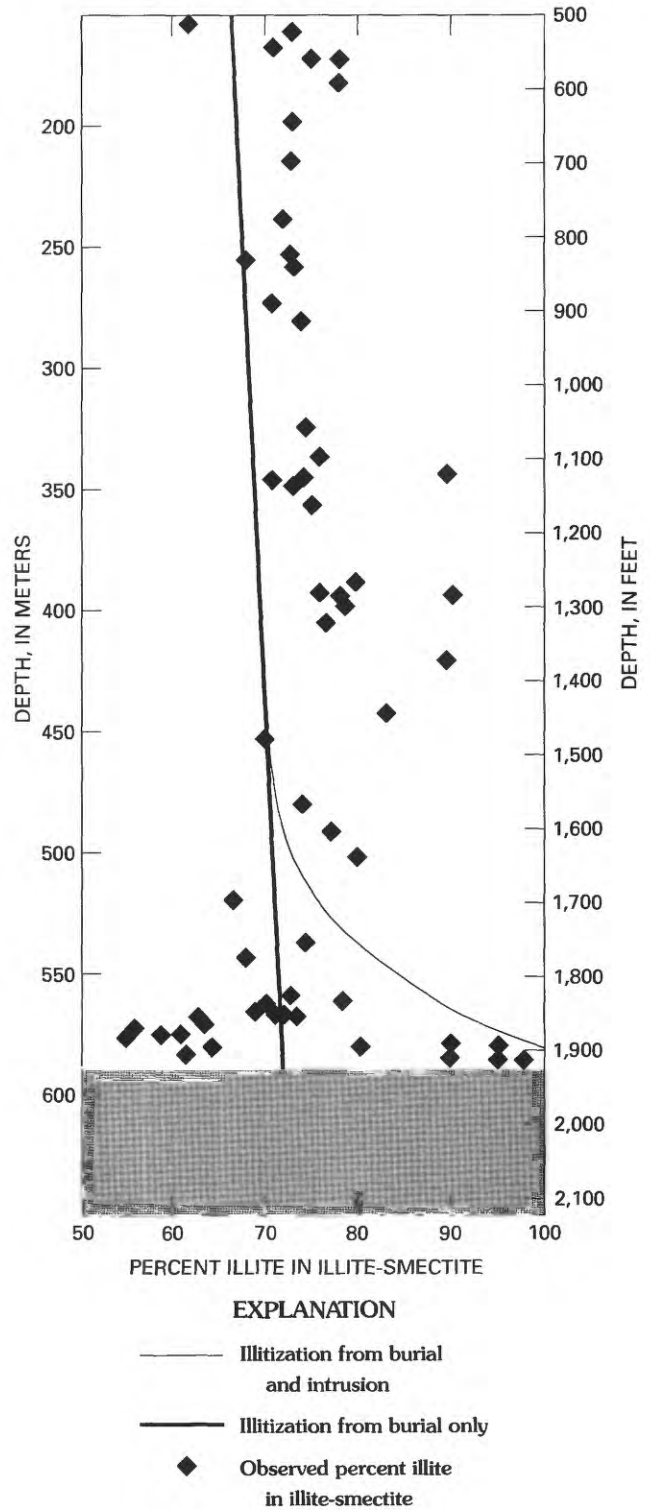


**Figure 30.** Comparison of calculated and observed percent illite in illite-smectite for core WC-83-5 using a 61-m-thick (200 ft), 1,200°C intrusion (shaded) for calculations. Illitization from burial only assumes burial depth of 4.1 km, geothermal gradient of 35°C/km, and depositional age of 40 million years.

## SUMMARY AND CONCLUSIONS

Thin igneous intrusions locally affected the thermal maturity of sedimentary rocks within a lithologically heterogeneous sedimentary basin in southwestern Washington. The expandability of illite-smectite decreases sharply in a narrow zone adjacent to each intrusion, whereas the abundance of kaolinite decreases as the abundance of chlorite increases and the amount of carbonate replacement increases near the intrusions. Alteration zones associated with the thin sills are very narrow and resulted from short-lived thermal pulses from the intrusions. Illite-smectite from two cores that contain intrusive bodies exhibits a greater extent of reaction throughout the core interval sampled (mean value for both cores is about 60 percent illite in illite-smectite,  $R=1$ ) compared to illite-smectite from the core containing no intrusions (almost fully expandable;  $\approx 0$ –10 percent illite in illite-smectite,  $R=0$ ).

Conductive modeling of the heat flow produced by the intrusions predicts short-lived and locally very intense heating. Sediments cooled to pre-intrusion temperatures only a few hundred years after the injection of these thin intrusions. Temperatures remained high enough to drive the kinetically controlled illitization reaction to a significant degree for only about 100 years. In the case of thin intrusions, the size of the illitization aureole was only slightly affected by variations in the intrusion temperature. Kinetic modeling suggests that substantial illitization ( $\approx 10$ –25 percent reduction in expandability) progressed in the host rock for a distance approximately equal to the thickness of the intrusion, matching the observed data tolerably well.

Finally, the regional pattern of thermal maturity reflected in coal grade throughout western Washington has probably been little affected by igneous intrusions. Even though a coal bed intruded by a sill would certainly exhibit strong thermal effects, the thermal maturity trends observed in coal on a regional scale probably resulted from thermal processes more widespread than the local heating produced by the thin igneous intrusions described herein.

## REFERENCES CITED

- Ahn, J.H., and Peacor, D.R., 1986, Transmission electron microscope data for rectorite—Implications for the origin and structure of “fundamental particles”: *Clays and Clay Minerals*, v. 34, p. 180–186.
- Altaner, S.P., 1989, Examination of models of smectite illitization [abs.]: *Clay Minerals Society Annual Meeting*, 26th, Sacramento, Calif., p. 13.
- Altaner, S.P., and Ylagan, R.F., 1993, Interlayer-by-interlayer dissolution—A new mechanism for smectite illitization [abs.]: *Clay Minerals Society Annual Meeting*, 30th, San Diego, Calif., p. 88.
- Armentrout, J.M., Hull, D.A., Beaulieu, J.D., and Rau, W.W., 1983, Correlation of Cenozoic stratigraphic units of western Oregon and Washington: State of Oregon Department of Geology and Mineral Industries, Oil and Gas Investigation 7, 90 p.
- Babcock, R.S., Burmester, R.F., Engebretson, D.C., Warnock, A., and Clark, K.P., 1992, A rifted margin origin for the Crescent Basalts and related rocks in the northern Coast Range volcanic province, Washington and British Columbia: *Journal of Geophysical Research*, v. 97, p. 6799–6821.
- Barton, M.D., Ilchik, R.P., and Marikos, M.A., 1992, Metasomatism, in Kerrick, D.M., ed., *Contact metamorphism: Mineralogical Society of America Reviews in Mineralogy*, v. 26, p. 321–350.
- Best, M.G., 1982, *Igneous and metamorphic petrology*: New York, W.H. Freeman, p. 630.
- Boles, J.R., and Franks, S.G., 1979, Clay diagenesis in Wilcox sandstone of southwest Texas, implications of smectite diagenesis on sandstone cementation: *Journal of Sedimentary Petrology*, v. 49, p. 55–70.
- Buckovic, W.A., 1979, The Eocene deltaic system of west-central Washington, in Armentrout, J.M., Cole, M.R., and TerBest, H., Jr., eds., *Pacific Coast Paleogeography Symposium 3: Society of Economic Paleontologists and Mineralogists*, p. 147–164.
- Buhmann, C., 1992, Smectite-to-illite conversion in a geothermally and lithologically complex Permian sedimentary sequence: *Clays and Clay Minerals*, v. 40, p. 53–64.
- Chang, H.K., Mackenzie, F.T., and Schoonmaker, J., 1986, Comparisons between the diagenesis of dioctahedral and trioctahedral smectite, Brazilian offshore basins: *Clays and Clay Minerals*, v. 34, p. 407–423.
- Couto Anjos, S.M., 1986, Absence of clay diagenesis in Cretaceous-Tertiary marine shales, Campos basin, Brazil: *Clays and Clay Minerals*, v. 34, p. 424–434.
- Drits, V.A., 1987, Mixed-layer minerals—Diffraction methods and structural features, in Schultz, L.G., van Olphen, H., and Mumpton, F.A., eds., *Proceedings of the International Clay Conference*, Denver: Bloomington, Indiana, The Clay Minerals Society, p. 33–45.
- Duncan, R.A., and Kulm, L.D., 1989, Plate tectonic evolution of the Cascades arc-subduction complex: *Geological Society of America, The Geology of North America*, v. N, The Eastern Pacific Ocean and Hawaii, p. 413–438.
- Eberl, D., and Hower, J., 1976, Kinetics of illite formation: *Geological Society of America Bulletin*, v. 87, p. 1326–1330.
- , 1977, The hydrothermal transformation of sodium and potassium smectite into mixed-layer clay: *Clays and Clay Minerals*, v. 25, p. 215–227.
- Eberl, D.D., and Srodon, J., 1988, Ostwald ripening and interparticle-diffraction effects for illite crystals: *American Mineralogist*, v. 73, p. 1335–1345.
- Eberl, D.D., Srodon, J., Kralik, M., Taylor, B.E., and Peterman, Z.E., 1990, Ostwald ripening of clays and metamorphic minerals: *Science*, v. 248, p. 474–477.
- Eberl, D.D., Whitney, G., and Houry, H., 1978, Hydrothermal reactivity of smectite: *American Mineralogist*, v. 63, p. 401–409.
- Evans, J.C., 1989, Facies analysis and sandstone diagenesis of the Carbonado Formation, western Washington: Fort Collins, Colorado State University, M.S. thesis, 172 p.

- Ewing, T.E., 1980, Paleogene tectonic evolution of the Pacific Northwest: *Journal of Geology*, v. 88, p. 619.
- Ferry, J.M., and Dipple, G.M., 1991, Fluid flow, mineral reactions, and metasomatism: *Geology*, v. 19, p. 211–214.
- Fisher, R.V., 1957, Stratigraphy of the Puget Group and Keechelus Group in the Elbe-Packwood area of southwestern Washington: Seattle, University of Washington, M.S. thesis, 151, p.
- 1961, Stratigraphy of the Ashford area, southern Cascades, Washington: *Geological Society of America Bulletin*, v. 72, p. 1395–1408.
- Frizzell, V.A., Jr., Tabor, R.W., Booth, D.B., Ort, K.M., and Waitt, R.B., Jr., 1984, Preliminary geologic map of the Snoqualmie Pass 1:100,000 quadrangle, Washington: United States Geological Survey Open-File Report 84–693.
- Furlong, K.P., Hanson, R.B., and Bowers, J.R., 1991, Modeling thermal regimes, in Kerrick, D.M., ed., *Contact metamorphism: Mineralogical Society of America Reviews in Mineralogy*, v. 26, p. 437–505.
- Hoffman, J., and Hower, J., 1979, Clay mineral assemblages as low grade metamorphic geothermometers, in Scholle, P.A., and Schluger, P.R., eds., *Aspects of diagenesis: Society of Economic Paleontologists and Mineralogists Special Publication 26*, p. 55–80.
- Howard, J.J., 1987, Influence of shale fabric on illite/smectite diagenesis in the Oligocene Frio Formation, south Texas, in Schultz, L.G., van Olphen, H., and Mumpton, F.A., eds., *Proceedings of the International Clay Conference*, Denver: Bloomington, Indiana, The Clay Minerals Society, p. 144–150.
- Howard, J.J., and Roy, D.M., 1985, Development of layer charge and kinetics of experimental smectite alteration: *Clays and Clay Minerals*, v. 33, p. 81–88.
- Hower, J., Eslinger, E.V., Hower, M.E., and Perry, E.A., 1976, Mechanism of burial metamorphism of argillaceous sediment—1. *Mineralogical and chemical evidence: Geological Society of America Bulletin*, v. 87, p. 725–737.
- Huang, W.L., 1992, Illitic-clay formation during experimental diagenesis of arkoses, in Houseknecht, D.W., and Pittman, E.D., eds., *Origin, diagenesis, and petrophysics of clay minerals in sandstones: Society of Economic Paleontologists and Mineralogists Special Publication 47*, p. 49–63.
- Huang, W.L., Longo, J.M., and Pevear, D.R., 1991, An experimentally derived kinetic model for smectite-to-illite conversion and its use as a geothermometer [abs.]: *Clay Minerals Society Annual Meeting*, 28th, Houston, Texas, p. 76.
- 1993, An experimentally derived kinetic model for smectite-to-illite conversion and its use as a geothermometer: *Clays and Clay Minerals*, v. 41, p. 162–177.
- Inoue, A., Kohyama, N., Kitagawa, R., and Watanabe, T., 1987, Chemical and morphological evidence for the conversion of smectite to illite: *Clays and Clay Minerals*, v. 35, p. 111–120.
- Inoue, A., and Utada, M., 1983, Further investigations of a conversion series of dioctahedral mica/smectites in the Shinzan hydrothermal alteration area, northeast Japan: *Clays and Clay Minerals*, v. 31, p. 401–412.
- Inoue, A., Utada, M., and Wakita, K., 1992, Smectite-to-illite conversion in natural hydrothermal systems: *Applied Clay Science*, v. 7, p. 131–145.
- Inoue, A., Velde, B., Meunier, A., and Touchard, G., 1988, Mechanism of illite formation during smectite-to-illite conversion in a hydrothermal system: *American Mineralogist*, v. 73, p. 1325–1334.
- Jackson, M.L., 1969, *Soil chemical analysis—Advanced course* (2nd ed.): Privately published, Madison, Wis., 895 p.
- Jaeger, J.C., 1964, Thermal effects of intrusions: *Reviews of Geophysics*, v. 2, p. 443–466.
- 1968, Cooling and solidification of igneous rocks, in Hess, H.H. and Poldwaart, A., eds., *Basalts: New York, John Wiley and Sons*, p. 503–536.
- Johnson, S.Y., 1984, Evidence for a margin-truncating transcurrent fault (pre-late Eocene) in western Washington: *Geology*, v. 12, p. 538–541.
- 1985, Eocene strike-slip faulting and non-marine basin formation in Washington, in Biddle, K.T., and Christie-Blick, N., eds., *Strike-slip deformation, basin formation and sedimentation: Society of Economic Paleontologists and Mineralogists Special Publication 37*, p. 283–302.
- Johnson, S.Y., and Yount, J.C., 1992, Toward a better understanding of the Paleogene paleogeography of the Puget Lowland, western Washington [abs.]: *Geological Society of America, Cordilleran Section, Annual Meeting*, 88th, Eugene, Oregon.
- Kerrick, D.M., 1991, Overview of contact metamorphism, in Kerrick, D.M., ed., *Contact metamorphism: Mineralogical Society of America Reviews in Mineralogy*, v. 26, p. 1–12.
- Laidler, K.J., and Meiser, J.H., 1982, *Physical chemistry: Menlo Park, Calif., Benjamin/Cummings*, p. 919.
- Lasaga, A.C., 1981, Rate laws of chemical reactions, in Lasaga, A.C., and Kirkpatrick, R.J., eds., *Kinetics of geochemical processes: Mineralogical Society of America Reviews in Mineralogy*, v. 8, p. 1–67.
- LeBas, M.J., Le Maitre, R.W., Streckeisen, A., and Zanettin, B., 1986, A chemical classification of volcanic rocks based on the total alkali-silica diagram: *Journal of Petrology*, v. 27, p. 745–750.
- Lovering, T.S., 1935, Theory of heat conduction applied to geological problems: *Geological Society of America Bulletin*, v. 46, p. 69–94.
- McCubbin, D.G., and Patton, J.W., 1981, Burial diagenesis of illite/smectite, a kinetic model [abs.]: *American Association of Petroleum Geologists Bulletin*, v. 65, p. 956.
- Moore, D.M., and Reynolds, R.C., 1989, *X-ray diffraction and the identification and analysis of clay minerals: Oxford University Press*, p. 332.
- Nadeau, P.H., Wilson, M.J., McHardy, W.J., and Tait, J.M., 1984, Interstratified clays as fundamental particles: *Science*, v. 225, p. 923–925.
- 1985, The conversion of illite during diagenesis—Evidence from some illitic clays from bentonites and sandstones: *Mineralogical Magazine*, v. 49, p. 393–400.
- Nilsen, T.H., and McKee, E.H., 1979, Paleogene paleogeography of the western United States, in Armentrout, J.M., Cole, M.R., TerBest, H., Jr., eds., *Pacific Coast Paleogeography Symposium 3: Society of Economic Paleontologists and Mineralogists*, p. 257–276.
- Perry, E.A., and Hower, J., 1970, Burial diagenesis in Gulf Coast pelitic sediments: *Clays and Clay Minerals*, v. 18, p. 165–177.
- Pollastro, R.M., 1982, A recommended procedure for the preparation of oriented clay-mineral specimens for X-ray diffraction analysis—Modifications to Drever's filter-membrane technique: *U.S. Geological Survey Open-File Report 82–71*, p. 24.

- 1985, Mineralogical and morphological evidence for the formation of illite at the expense of illite/smectite: *Clays and Clay Minerals*, v. 33, p. 265–274.
- 1993, Considerations and applications of the illite/smectite geothermometer in hydrocarbon bearing rocks of Miocene to Mississippian age: *Clays and Clay Minerals*, v. 41, p. 119–133.
- Pytte, A.M., 1982, The kinetics of the smectite to illite reaction in contact metamorphic shales: Hanover, N.H., Dartmouth University, M.S. thesis, p. 78.
- Pytte, A.M., and Reynolds, R.C., Jr., 1989, The thermal transformation of smectite to illite, in Naeser, N.D., and McCulloh, T.H., eds., *Thermal history of sedimentary basins, methods, and case histories*: New York, Springer-Verlag, p. 133–140.
- Ramseyer, K., and Boles, J.R., 1986, Mixed-layer illite/smectite minerals in Tertiary sandstones and shales, San Joaquin Basin, California: *Clays and Clay Minerals*, v. 34, p. 115–124.
- Reynolds, R.C., Jr., 1980, Interstratified clay minerals, in Brindley, G.W., and Brown, G., eds., *Crystal structures of clay minerals and their X-ray identification*: London, Mineralogical Society, p. 495.
- 1985, NEWMOD—A computer program for the calculation of one-dimensional diffraction patterns of mixed-layer clays: 8 Brook Dr., Hanover, N.H.
- Roberson, H.E., and Lahann, R.W., 1981, Smectite to illite conversion rates—Effects of solution chemistry: *Clays and Clay Minerals*, v. 29, p. 129–135.
- Sheih, Y.N., and Taylor, H.P., 1969, Oxygen and hydrogen isotope studies of contact metamorphism in the Santa Rosa Range, Nevada and other areas. *Contributions to Mineralogy and Petrology*, v. 20, p. 306–356.
- Snavely, P.D., Jr., 1988, Tertiary geologic framework, neotectonics, and petroleum potential of the Oregon-Washington continental margin, in Scholl, D.S., Grantz, A., and Vedder, J.G., eds., *Geology and resource potential of the continental margin of western North America and adjacent ocean basins—Beaufort Sea to Baja, California*: Circum-Pacific Council for Energy and Mineral Resources Earth Science Series, v. 6, p. 305–335.
- Srodon, J., 1980, Precise identification of illite/smectite interstratifications by X-ray powder diffraction: *Clays and Clay Minerals*, v. 28, p. 401–411.
- Summer, N.S., and Verosub, K.L., 1989, A low temperature hydrothermal maturation mechanism for sedimentary basins associated with volcanic rocks, in Price, R.A., ed., *Origin and evolution of sedimentary basins and their energy and mineral resources*: American Geophysical Union Geophysical Monograph 48, International Union of Geodesy and Geophysics, v. 3, p. 129–136.
- Tertian, R., and Claisse, F., 1982, *Principles of quantitative X-ray fluorescence analysis*: London, Hayden and Sons Ltd., 385 p.
- Turner, D.L., Frizzell, V.A., Jr., Triplehorn, D.M., and Naeser, C.W., 1983, Radiometric dating of ash partings in coal of the Eocene Puget Group, Washington—Implications for paleobotanical stages: *Geology*, v. 11, p. 527–531.
- Velde, B., and Lanson, B., 1993, Comparison of I/S transformation and maturity of organic matter at elevated temperatures: *Clays and Clay Minerals*, v. 41, p. 178–183.
- Velde, B., and Vasseur, G., 1992, Estimation of the diagenetic smectite to illite transformation in time-temperature space: *American Mineralogist*, v. 77, p. 967–976.
- Vine, J.D., 1962, Stratigraphy of Eocene rocks in a part of King County, Washington: Washington Division of Mines and Geology, Report of Investigation, 21 p.
- Walsh, T.J., and Lingley, W.S., Jr., 1991, Coal maturation and the natural gas potential of western and central Washington: Washington Division of Geology and Earth Resources Open-File Report 91–2, 26 p.
- Walsh, T.J., and Phillips, W.M., 1983, Rank of Eocene coals in western Washington State—A reflection of Cascade Plutonism?: Washington Division of Geology and Earth Resources Open-File Report 83–16, 21 p.
- Waples, D.W., 1985, *Geochemistry in petroleum exploration*: Boston, International Human Resources Development Corporation, p. 217.
- Weaver, C.E., and Beck, K.C., 1971, Clay water diagenesis during burial—How mud becomes gneiss: *Geological Society of America Special Paper 134*, p. 96.
- Wells, R.E., Engebretson, D.C., Snavely, P.D., Jr., and Coe, R.S., 1984, Cenozoic plate motions and the volcano-tectonic evolution of western Oregon and Washington: *Tectonics*, v. 3, p. 275–294.
- Wells, R.E., and Heller P.L., 1988, The relative contribution of accretion, shear, and extension to Cenozoic tectonic rotation in the Pacific Northwest: *Geological Society of America Bulletin*, v. 100, p. 325–338.
- Whitney, G., 1983, Hydrothermal reactivity of saponite: *Clays and Clay Minerals*, v. 31, p. 1–8.
- 1990, Role of water in the smectite to illite reaction: *Clays and Clay Minerals*, v. 38, p. 343–350.
- 1992, Dioctahedral smectite reactions at elevated temperatures—Effects of K-availability, Na/K ratio and ionic strength: *Applied Clay Science*, v. 7, p. 97–112.
- Whitney, G., and Northrop, H.R., 1988, Experimental investigation of the smectite to illite reaction—Dual reaction mechanisms and oxygen-isotope systematics: *American Mineralogist*, v. 73, p. 77–90.
- Whitney, G., and Velde, B., 1993, Changes in particle morphology during illitization—An experimental study: *Clays and Clay Minerals*, v. 41, p. 209–218.
- Yau, Y., Peacor, D.R., and McDowell, S.D., 1987, Smectite-to-illite reactions in Salton Sea shales—A transmission and analytical electron microscopy study: *Journal of Sedimentary Petrology*, v. 57, p. 335–342.

---

---

## APPENDIX

---

---

**Appendix table 1.** Major-element chemical analyses for samples from core WC-83-6.  
 [Location of core hole shown in text figure 1. Samples shown in italics are igneous rocks]

Sample number	Depth (feet)	SiO <sub>2</sub> (percent)	Al <sub>2</sub> O <sub>3</sub> (percent)	FeTO <sub>3</sub> (percent)	MnO (percent)	MgO (percent)	CaO (percent)	Na <sub>2</sub> O (percent)	K <sub>2</sub> O (percent)	TiO <sub>2</sub> (percent)	P <sub>2</sub> O <sub>5</sub> (percent)	Total (percent)	Igneous type	Thickness (feet)
85	1,263	63.16	19.32	4.11	0.05	1.71	1.78	2.32	2.04	0.89	0.30	95.68		
84	1,270.2	66.62	18.17	4.98	0.06	1.91	0.83	2.12	2.37	0.83	0.24	98.13		
83	1,271.6	63.31	17.47	7.71	0.11	2.32	0.77	1.85	2.25	0.83	0.30	96.92		
82	1,273.2	63.97	21.18	4.46	0.03	2.09	0.64	1.90	2.95	0.86	0.15	98.23		
81	1,273.8	63.07	20.33	4.55	0.03	2.11	0.58	1.82	2.80	0.84	0.16	96.29		
<i>Flow H</i>	<i>1,278</i>	<i>66.52</i>	<i>17.87</i>	<i>7.45</i>	<i>0.17</i>	<i>2.33</i>	<i>9.91</i>	<i>3.27</i>	<i>0.89</i>	<i>0.78</i>	<i>0.14</i>	<i>99.33</i>	<i>Flow</i>	8.4
<i>Flow G</i>	<i>1,281.4</i>	<i>53.47</i>	<i>18.97</i>	<i>8.23</i>	<i>0.24</i>	<i>2.62</i>	<i>11.73</i>	<i>3.21</i>	<i>0.49</i>	<i>0.87</i>	<i>0.12</i>	<i>99.95</i>	<i>Flow</i>	2.2
80	1,282.5	65.74	18.52	4.47	0.03	2.13	0.60	1.74	2.76	0.73	0.23	96.95		
79	1,283	66.82	16.71	6.18	0.07	2.12	1.26	1.59	2.40	0.75	0.29	98.19		
78	1,283.5	67.62	17.45	5.37	0.06	1.97	1.05	1.58	2.42	0.77	0.27	98.56		
77	1,305.2	57.86	16.28	14.74	0.34	2.57	1.84	1.80	2.23	0.87	0.38	98.91		
76	1,313.6	53.10	24.24	9.31	0.03	1.19	4.23	3.21	0.91	1.64	0.38	98.24		
74	1,317.4	59.50	20.61	8.78	0.05	2.22	0.42	1.57	2.88	0.81	0.20	97.04		
73	1,318.8	71.05	14.87	3.37	0.06	1.47	0.90	2.39	1.95	0.63	0.24	96.93		
72	1,336	66.06	17.88	7.42	0.10	2.05	0.72	2.00	2.52	0.88	0.28	99.91		
75	1,341	63.51	18.82	7.50	0.08	1.67	0.81	1.36	3.24	0.96	0.31	98.26		
71	1,353	66.17	16.34	5.57	0.05	1.50	1.03	1.77	2.38	0.74	0.35	95.90		
70	1,353.5	59.88	22.49	5.97	0.07	1.62	1.52	2.25	2.43	1.21	0.39	97.83		
69	1,362.5	66.56	12.04	3.58	0.15	1.12	9.87	2.00	1.63	0.47	0.20	97.62		
68	1,378.5	67.09	17.68	6.06	0.07	1.79	0.73	2.14	2.79	0.82	0.25	99.42		
67	1,400	64.00	17.93	10.68	0.30	2.03	1.12	1.74	2.67	1.10	0.30	101.87		
66	1,402.8	61.54	18.89	8.99	0.18	2.35	1.36	1.96	2.68	0.92	0.26	99.13		
65	1,446.8	77.64	12.54	2.29	0.04	0.76	0.93	2.17	2.19	0.34	0.16	99.06		
64	1,463.6	76.87	13.26	2.85	0.05	0.96	1.36	3.15	2.33	0.48	0.17	101.48		
63	1,466.5	74.42	13.47	2.60	0.05	1.10	1.25	2.31	2.17	0.40	0.18	97.95		
62	1,469.2	78.03	12.15	1.68	0.06	0.71	2.49	2.36	2.13	0.31	0.16	100.08		
61	1,470	76.58	12.81	2.08	0.05	0.92	1.85	2.16	2.12	0.33	0.17	99.07		
60	1,470.4	76.27	13.28	3.04	0.05	1.20	1.04	2.80	2.26	0.47	0.17	100.58		
<i>Intrusion F</i>	<i>1,494</i>	<i>59.79</i>	<i>15.88</i>	<i>7.59</i>	<i>0.11</i>	<i>4.94</i>	<i>6.10</i>	<i>4.01</i>	<i>1.35</i>	<i>0.93</i>	<i>0.14</i>	<i>100.84</i>	<i>Intrusion</i>	31.3
59	1,501.9	71.19	11.17	4.06	0.26	1.61	8.64	1.84	1.41	0.41	0.16	100.75		
58	1,503.3	77.14	10.48	2.34	0.12	1.12	4.48	2.78	1.53	0.20	0.14	100.33		
57	1,504.3	67.78	15.29	6.20	0.10	2.14	3.04	2.20	1.65	0.63	0.22	99.25		
<i>Flow E</i>	<i>1,501</i>	<i>44.28</i>	<i>16.49</i>	<i>15.83</i>	<i>0.63</i>	<i>5.62</i>	<i>14.48</i>	<i>3.06</i>	<i>0.44</i>	<i>1.05</i>	<i>0.09</i>	<i>101.97</i>	<i>Flow</i>	1.7
56	1,505.5	67.25	14.76	6.70	0.10	2.70	2.46	2.85	1.77	0.71	0.27	99.57		
55	1,506.2	64.25	18.02	6.60	0.07	2.27	1.34	2.56	2.74	0.89	0.26	99.00		
54	1,507.2	56.55	15.12	16.59	0.16	2.57	1.13	1.96	2.26	0.81	0.22	97.37		
53	1,546.5	58.28	24.37	3.50	0.04	2.87	1.55	1.60	3.63	0.38	0.14	96.36		
52	1,554.8	63.17	17.75	5.08	0.05	2.19	0.77	2.46	2.53	0.82	0.22	95.04		
51	1,558.5	64.79	19.00	4.97	0.04	1.97	0.65	1.69	2.98	0.95	0.25	97.29		

Appendix table 1. Major-element chemical analyses for samples from core WC-83-6—Continued.

Sample number	Depth (feet)	SiO <sub>2</sub> (percent)	Al <sub>2</sub> O <sub>3</sub> (percent)	Fe <sub>2</sub> O <sub>3</sub> (percent)	MnO (percent)	MgO (percent)	CaO (percent)	Na <sub>2</sub> O (percent)	K <sub>2</sub> O (percent)	TiO <sub>2</sub> (percent)	P <sub>2</sub> O <sub>5</sub> (percent)	Total (percent)	Igneous type	Thickness (feet)
50	1,578.7	73.27	13.60	3.80	0.05	1.18	1.09	2.20	2.28	0.59	0.21	98.27		
49	1,601	68.06	15.06	4.24	0.05	1.40	1.18	2.24	2.35	0.61	0.20	95.39		
48	1,611	76.53	10.25	1.84	0.20	0.58	5.55	2.27	1.74	0.21	0.15	99.32		
47	1,613.3	67.10	17.86	5.07	0.02	1.47	0.63	2.08	3.48	0.82	0.26	98.79		
46	1,651	65.14	13.42	4.84	0.15	2.55	5.31	2.11	1.69	0.51	0.21	95.93		
45	1,654.5	70.16	16.95	5.30	0.05	1.42	0.54	1.90	2.73	0.87	0.28	100.20		
44	1,655.5	65.57	20.51	4.57	0.03	1.65	0.38	1.47	3.28	0.95	0.20	98.61		
<i>Intrusion D</i>	<i>1,672</i>	<i>51.23</i>	<i>18.59</i>	<i>10.48</i>	<i>0.17</i>	<i>6.51</i>	<i>5.84</i>	<i>3.42</i>	<i>0.84</i>	<i>0.91</i>	<i>0.05</i>	<i>98.04</i>	<i>Intrusion</i>	<i>28</i>
43	1,700	66.39	16.87	4.71	0.06	1.79	0.70	2.05	2.62	0.71	0.26	96.16		
42	1,722.6	68.66	14.40	4.36	0.09	1.24	3.87	1.80	2.14	0.58	0.23	97.37		
41	1,743.5	65.37	18.14	5.92	0.09	1.62	0.99	1.49	2.72	0.87	0.29	97.50		
40	1,760	70.89	14.08	3.90	0.06	1.24	1.94	2.40	2.28	0.46	0.23	97.48		
39	1,766	61.45	12.40	3.85	0.22	1.31	14.89	1.73	1.57	0.63	0.23	98.28		
38	1,768.8	63.72	17.56	6.04	0.07	1.97	0.78	2.16	3.03	0.78	0.28	96.39		
37	1,769.8	68.21	17.03	5.00	0.04	1.79	0.62	1.83	2.98	0.74	0.24	98.48		
36	1,778	69.53	17.06	5.83	0.05	1.76	0.76	1.50	2.74	0.86	0.25	100.34		
<i>Intrusion C</i>	<i>1,801</i>	<i>51.43</i>	<i>16.57</i>	<i>10.16</i>	<i>0.16</i>	<i>4.07</i>	<i>10.39</i>	<i>3.06</i>	<i>0.56</i>	<i>1.3</i>	<i>0.18</i>	<i>97.88</i>	<i>Intrusion</i>	<i>19.5</i>
35	1,804.5	61.90	18.18	6.30	0.07	2.65	2.15	1.82	2.04	0.94	0.33	96.38		
34	1,805.3	65.89	18.18	4.77	0.04	2.07	1.05	1.82	2.89	0.85	0.33	97.89		
33	1,806	64.65	17.18	6.34	0.04	2.58	0.76	1.90	2.31	0.81	0.31	96.88		
32	1,807.3	68.55	16.39	5.21	0.05	1.83	1.12	1.70	2.29	0.78	0.32	98.24		
31	1,808.8	65.83	16.56	5.30	0.06	1.88	1.37	1.77	2.32	0.79	0.28	96.16		
30	1,810.8	63.74	16.26	4.49	0.14	1.77	5.96	1.61	2.03	0.75	0.27	97.02		
28	1,814.7	69.24	15.59	5.71	0.07	1.82	1.85	2.15	2.24	0.73	0.33	99.73		
27	1,816.7	63.45	19.55	6.05	0.06	2.10	0.63	1.57	2.97	0.90	0.32	97.60		
26	1,828.4	49.94	12.80	7.14	0.31	3.41	23.86	1.03	0.94	0.66	0.25	100.34		
25	1,854.8	60.69	16.80	8.59	0.15	2.68	5.28	1.35	1.92	0.88	0.41	98.75		
<i>Intrusion B</i>	<i>1,903.3</i>	<i>51.21</i>	<i>16.96</i>	<i>9.74</i>	<i>0.22</i>	<i>3.66</i>	<i>13.00</i>	<i>2.31</i>	<i>0.43</i>	<i>1.28</i>	<i>0.31</i>	<i>99.12</i>	<i>Intrusion</i>	<i>10</i>
23	1,928.5	67.79	18.38	4.50	0.04	1.75	0.54	1.71	2.64	0.84	0.28	98.47		
22	1,940.7	66.46	13.30	6.37	0.12	2.61	5.48	2.11	1.50	0.47	0.24	98.66		
21	1,944	54.60	17.78	9.13	0.19	3.58	9.03	2.30	0.71	1.34	0.34	99.00		
<i>Flow A</i>	<i>1,945</i>	<i>51.47</i>	<i>16.75</i>	<i>9.99</i>	<i>0.24</i>	<i>4.10</i>	<i>11.52</i>	<i>3.00</i>	<i>0.50</i>	<i>1.25</i>	<i>0.20</i>	<i>99.02</i>	<i>Flow</i>	<i>3.7</i>
19	1,953	70.19	17.01	6.37	0.09	1.38	0.97	1.70	2.51	0.93	0.18	101.33		
18	1,962.8	72.05	14.54	4.34	0.07	1.22	3.23	2.36	1.49	0.58	0.22	100.10		
17	1,965.4	67.94	11.32	7.83	0.09	3.81	2.82	2.98	0.91	0.43	0.16	98.29		
16	1,991	66.27	19.91	5.07	0.06	1.59	0.60	1.88	3.13	0.96	0.29	99.76		
15	1,999	56.96	18.05	7.83	0.09	4.21	6.68	3.47	0.74	1.18	0.54	99.75		

Appendix table 2. Major-element chemical analyses for samples from core WC-83-5 and WC-83-6. [Location of core holes shown in text figure 1]

Core	Sample	Sample depth (feet)	Midpoint of igneous sheet (feet)	Intrusion thickness (feet)	SiO <sub>2</sub>	Al <sub>2</sub> O <sub>3</sub>	FeTO <sub>3</sub>	MnO	MgO	CaO	Na <sub>2</sub> O	K <sub>2</sub> O	TiO <sub>2</sub>	P <sub>2</sub> O <sub>5</sub>	Total	Igneous type
WC-83-5	Flow L	1,115.3	1,120.5	10.0	51.68	16.82	9.42	0.12	5.63	11.35	2.45	0.51	1.21	0.18	99.37	Flow
WC-83-5	Flow K	1,264.5	1,264.5	10.8	50.27	16.45	10.47	0.14	7.07	10.16	2.52	0.50	1.37	0.13	99.08	Flow
WC-83-5	Flow J	1,276	1,274.9	5.2	49.02	15.74	11.33	0.17	7.94	11.20	2.35	0.41	1.32	0.16	99.64	Flow
WC-83-5	Intrusion I	1,973	1,955.2	>84	51.31	18.82	9.17	0.14	6.19	5.62	5.75	0.98	1.38	0.20	99.56	Pluton (?)
WC-83-6	Flow H	1,278	1,276.5	8.4	56.52	17.87	7.45	0.17	2.33	9.91	3.27	0.89	0.78	0.14	99.33	Flow
WC-83-6	Flow G	1,281.4	1,281.4	2.2	53.47	18.97	8.23	0.24	2.62	11.73	3.21	0.49	0.87	0.12	99.95	Flow
WC-83-6	Intrusion F	1,494.8	1,486.2	31.3	59.79	15.88	7.59	0.11	4.94	6.10	4.01	1.35	0.93	0.14	100.84	Intrusion
WC-83-6	Flow E	1,505.4	1,505.2	1.7	44.28	16.49	15.83	0.63	5.62	14.48	3.06	0.44	1.05	0.09	101.97	Flow
WC-83-6	Intrusion D	1,672	1,674.5	28.0	51.23	18.59	10.48	0.17	6.51	5.84	3.42	0.84	0.91	0.05	98.04	Intrusion
WC-83-6	Intrusion C	1,801	1,794.8	19.5	51.43	16.57	10.16	0.16	4.07	10.39	3.06	0.56	1.3	0.18	97.88	Intrusion
WC-83-6	Intrusion B	1,903.3	1,892	10.0	51.21	16.96	9.74	0.22	3.66	13.00	2.31	0.43	1.28	0.31	99.12	Intrusion
WC-83-6	Flow A	1,945	1,945.6	3.7	51.47	16.75	9.99	0.24	4.10	11.52	3.00	0.50	1.25	0.20	99.02	Flow



